Received: 6 August 2023 | Revised: 6 November 2023 | Accepted: 13 November 2023

DOI: 10.1002/eqe.4049

WILEY

RESEARCH ARTICLE

Convolutional neural network for identifying effective seismic force at a DRM layer for rapid reconstruction of SH ground motions

Shashwat Maharjan[1] | **Bruno Guidio**[1] | **Chanseok Jeong**[1,2]

[1]School of Engineering and Technology, Central Michigan University, Mount Pleasant, Michigan, USA

[2]Earth and Ecosystem Science Program, Central Michigan University, Mount Pleasant, Michigan, USA

Correspondence
Chanseok Jeong, School of Engineering and Technology, Central Michigan University, Mount Pleasant, MI 48859, USA.
Email: jeong1c@cmich.edu

Funding information
Faculty Research and Creative Endeavors, Grant/Award Number: 48058; Extreme Science and Engineering Discovery Environment; National Science Foundation, Grant/Award Numbers: CMMI-2053694, ACI-1548562, ACI-1928147

Abstract

We introduce a novel data-informed convolutional neural network (CNN) approach that utilizes sparse ground motion measurements to accurately identify effective seismic forces in a truncated two-dimensional (2D) domain. Namely, this paper presents the first prototype of a CNN capable of inferring domain reduction method (DRM) forces, equivalent to incident waves, across all nodes in the DRM layer. It achieves this from sparse measurement data in a multidimensional setting, even in the presence of incoherent incident waves. The method is applied to shear (SH) waves propagating into a domain truncated by a wave-absorbing boundary condition (WABC). By effectively training the CNN using input-layer features (surface sensor measurements) and output-layer features (effective forces at a DRM layer), we achieve significant reductions in processing time compared to PDE-constrained optimization methods. The numerical experiments demonstrate the method's effectiveness and robustness in identifying effective forces, equivalent to incoherent incident waves, at a DRM layer.

KEYWORDS

convolutional neural network, domain reduction method, incident seismic motion inversion, inverse-source problem, machine learning, seismic wave propagation

1 | INTRODUCTION

Being able to reconstruct wave motions, in a domain of interest including soils and built environments, using sparsely measured ground motion data is resourceful for identifying the locations of dynamic responses of significant amplitudes during a seismic event. Engineers can use this technique to make precise estimates of the impact of earthquakes on soils and critical structures, identifying weak spots or areas that may be at risk of damage. Current practices, which utilize ground measurements for estimating the seismic waves impinging a domain of interest, as a prior step to the reconstruction of the wave responses in the domain, typically rely on (i) the deconvolution procedure in a soil column,[1–4] (ii) the seismic source identification in a large-scale domain,[5,6] (iii) output only blind identification,[7,8] (iv) Bayesian finite element (FE) model updating,[9,10] and (v) multiwavefield inversion.[11] When it comes to deconvolution, the technique is reliable only in scenarios where a soil column is horizontally layered, and the seismic waves propagate vertically through a one-dimensional (1D) medium.

On the other hand, the efficiency and accuracy of the large-scale source inversion procedure are hindered by the high computational cost, especially for high-frequency contents (e.g., higher than 2 Hz), and the uncertainties in material properties across a vast domain. It is because the large-scale forward modeling has to model waves from a source to structures in the domain with known wave speeds. Output-only blind identification methods were investigated to identify the transfer functions of soil columns and vertically propagating incident waves, accounting for geophysical uncertainty by analyzing measured ground motion signals from multiple stations, but only vertically propagating incident waves have been considered. Bayesian estimation method has also been studied for the FE model updating of the nonlinear soil properties in a soil column and the characterization of the vertically propagating incoming seismic wave toward the column.[9] Such a Bayesian FE model estimation method was extended to a problem where the structural properties of an instrumented building and its foundation input motion at the nodal points of the foundation slab are identified during a seismic event.[10] The nodal points of the foundation slab are modeled with 3-axis linear springs and 3-axis linear viscous dampers. However, the Bayesian FE model estimation method has not been reported to be applicable to the reconstruction of the dynamic motions of a volume of soils surrounding a building subject to arbitrarily propagating waves. Li et al.[11] emphasized the importance of inverting body wave profiles for a realistic assessment of seismic effects on structures. However, their multiwavefield-inversion methodology only estimates the incident angle of an idealized plane wave.

To complement the aforementioned existing techniques in terms of applicability and computational resources, Guidio et al.[12] have recently introduced a new method, powered by the partial differential equation (PDE)-constrained optimization, for estimating incoming shear (SH) motions of a plane waveform, modeled as moving traction on wave absorbing boundaries, using observational data from ground sensors. As opposed to the large-scale source-inversion method, this seismic input identification approach only relies on the wave speed data from a near-surface truncated deposit, which can be easily acquired using site characterization techniques like spectral analysis of surface waves (SASW),[13–17] multichannel analysis of surface waves (MASW),[18,19] or full-waveform inversion (FWI).[20,21] Guidio et al.[22] presented another method to estimate dynamic nodal forces, which represent arbitrary forms of incoming waves, within a domain reduction method (DRM) layer in a truncated domain by using measurement data. It is noteworthy that the DRM theory was developed by Bielak et al.[23] and Yoshimura et al.[24] to translate the incoming, incident seismic motions into effective seismic nodal forces on the DRM layer (i.e., virtual interfaces) of a domain of interest. In other words, when it comes to modeling the wave responses in a truncated domain subject to waves originating from the outside of the domain, such effective seismic nodal forces on a DRM layer drive the wave motions in the domain. Because of its robustness and extensive applicability, the DRM has been widely utilized in numerous research investigations to simulate seismic behaviors in truncated domains.[25–36]

While the PDE-constrained optimization is highly effective in estimating seismic inputs, in the form of DRM forces, in 2D settings, it is still burdened by time-consuming processes, hindering real time processing, because each inversion simulation typically requires hundreds of forward and adjoint wave simulations in the domain. Such an approach in multidimensional settings would not be a practical, viable tool for rapid reconstruction of wave responses in a domain of interest. Therefore, we examine the efficiency and reliability of utilizing machine learning (ML) for the incident wave (or equivalent DRM forces) inversion problem. This approach aims to significantly reduce processing time so that the seismic responses of built environments and surrounding soils can be rapidly reconstructed, being informative to decision makers.

The literature on the application of ML for solving inverse problems has seen a recent increase. Gokhale[37] investigated the utilization of convolutional neural networks (CNNs) to reconstruct the shear modulus field in an isotropic, linear elastic medium under plane strain conditions. Their study focuses on using displacement data to effectively recover the shear modulus in a domain, highlighting the generalization potential of CNNs. Vantassel et al.[38] explored the application of a CNN to create a two-dimensional (2D) material profile using surface measurements caused by a wave source located at the surface. The obtained material profile was subsequently employed as the initial input for the subsequent FWI process. Stankevich et al.[39] addressed the challenge of acquiring velocity models for complex media by employing CNNs. Their approach solely relies on boundary measurements, with a specific focus on the variations commonly encountered in seismic exploration. In a similar context, Wu et al.[40] proposed a deep CNN architecture with an encoder–decoder structure. The encoder component learns an abstract representation of seismic waveforms, which is subsequently utilized by the decoder to generate a subsurface model based on synthetic seismic waveform data. Furthermore, regarding the seismic input wave motion prediction problem, Maharjan et al.[41] designed deep and CNN architectures. Their models effectively predict the incoming wave motion in a 1D soil column based on surface measurements. The authors showcased the effectiveness and robustness of their approaches through rigorous testing.

This paper draws inspiration from the promising application of ML for seismic input inversion in a 1D soil column as presented by Maharjan et al.[41] Building upon the previous work, this study utilizes a novel data-informed CNN approach

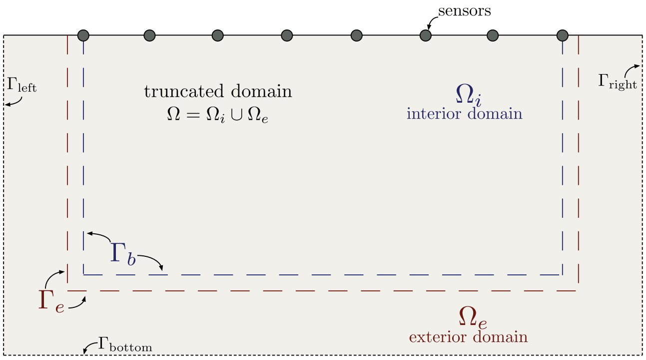

FIGURE 1 Problem configuration: a 2D reduced domain Ω truncated by WABC on Γ_{left}, Γ_{bottom}, and Γ_{right}. Γ_b and Γ_e delineate a single-element thick DRM layer.

for identifying effective seismic forces at a DRM layer in a truncated 2D domain using ground surface measurements. The presented method aims to significantly reduce the processing time[1] required for identifying DRM forces and reconstructing ground motions within a domain once an ANN is trained.

The structure of the paper is organized as the following. We present a method for generating synthetic training data using a randomizer-based forward wave simulator. This data includes input-layer features, such as ground-surface displacement measurements, and output-layer features, specifically effective seismic forces within the DRM layer. We proceed to train a CNN and assess its efficacy in solving the DRM-force inversion problem.

2 | PROBLEM DESCRIPTION

2.1 | Objective of the presented CNN

This research paper delves into a CNN method that relates ground-surface seismic motion measurements to effective seismic forces (i.e., equivalent dynamic nodal forces that replicate incoming seismic waves imparted from the outside of a domain) at two virtual interfaces (i.e., Γ_b and Γ_e) of a DRM layer within a near-surface 2D domain (Ω) truncated by wave-absorbing boundary condition (WABC), as depicted in Figure 1. The domain is occupied by a linear, elastic, and undamped solid.

Under the presented CNN approach, the output-layer features that we aim to identify are the values of a set of $P_{b_{kj}}$ and $P_{e_{kj}}$. They are components of nodal forces, respectively, corresponding to the kth node on Γ_b (or Γ_e) and the jth time step. The subscript k increments as we proceed in a counterclockwise direction, counting the nodes on the interfaces Γ_b or Γ_e, starting from the upper-left node of each interface. We also note that the thickness of the DRM layer is the length of one edge of a typical finite element, discretizing the domain, per the original DRM theory.

2.2 | Wave physics considered for the reconstruction of wave responses in the truncated domain after the potential identification of DRM forces by the CNN

The 2D domain of interest Ω is subject to scalar wave (SH) motions, which are governed by the following PDE:

$$\nabla \cdot (G\nabla u) - \rho \frac{\partial^2 u}{\partial t^2} = 0. \tag{1}$$

In the above, $u := u(x, y, t)$ denotes the displacement field of a solid particle located at x and y under wave motions in the antiplane direction (i.e., the z direction) on time $t \in \mathrm{J} = (0, T]$, in which T is the observation period; $G(x, y)$ and $\rho(x, y)$

---

[1] Please note that the training time is not counted toward the processing time.

are the shear modulus and mass density of the solid, respectively. The top (Γ_{top}), left (Γ_{left}), bottom (Γ_{bottom}), and right (Γ_{right}) boundaries of the domain Ω are subject to the following boundary conditions:

$$\frac{\partial u}{\partial y} = 0, \qquad \text{on } \Gamma_{\text{top}}, \tag{2a}$$

$$\frac{\partial u}{\partial x} = -\frac{1}{V_{\text{s}}}\frac{\partial u}{\partial t}, \qquad \text{on } \Gamma_{\text{left}},\ \Gamma_{\text{right}}, \tag{2b}$$

$$\frac{\partial u}{\partial y} = -\frac{1}{V_{\text{s}}}\frac{\partial u}{\partial t}, \qquad \text{on } \Gamma_{\text{bottom}}, \tag{2c}$$

where $V_{\text{s}}(x, y) = \sqrt{G(x, y)/\rho(x, y)}$ refers to the shear wave velocity of the domain. Specifically, Γ_{top} is subject to traction-free condition, while the other boundaries (Γ_{left}, Γ_{bottom}, and Γ_{right}) are subject to WABC.[42]

To obtain numerical solutions for the considered problem setting, we apply the finite element method (FEM) to Equation (1), considering the boundary conditions in Equation (2). Then, we formulate the strong form, through the weak form, into the following time-dependent semi-discrete equation:

$$\mathbf{K}\mathbf{u}(t) + \mathbf{C}\dot{\mathbf{u}}(t) + \mathbf{M}\ddot{\mathbf{u}}(t) = \mathbf{F}(t), \tag{3}$$

where $\mathbf{K}$, $\mathbf{C}$, and $\mathbf{M}$ represent the global stiffness, damping, and mass matrices, respectively; $\mathbf{u}(t)$, $\dot{\mathbf{u}}(t)$, and $\ddot{\mathbf{u}}(t)$ are the displacement, velocity, and acceleration solution vectors at time t, respectively; and $\mathbf{F}(t)$ denotes the global force vector at time t. For brevity, we omit to show the details of the matrices. This work solves Equation (3) using the implicit Newmark time integration scheme.

Without any external traction defined in the aforementioned boundary condition or any body force in Equation (1), $\mathbf{F}(t)$ should vanish. However, in a forward wave problem under the original DRM theory, incident seismic waves can be modeled as effective seismic forces (i.e., nodal forces on Γ_b and Γ_e) within $\mathbf{F}(t)$, driving the dynamic motions in the domain Ω. In our presented wave-response reconstruction problem, the CNN-predicted effective seismic forces (i.e., nodal forces on Γ_b and Γ_e at discrete time steps that are identified from our CNN) will constitute the global force vector $\mathbf{F}$ at the discrete time steps. In other words, after the accurate identification of the targeted DRM forces at all time steps by the CNN and plugging them into $\mathbf{F}$, we can reconstruct the wave responses in the truncated domain, subject to targeted incident waves, at each time step via the time integration scheme.

3 | METHODS

3.1 | Data generation

To generate training data for the CNN, we design a randomizer that solves a forward shear (SH) wave problem considering that a relatively small-sized truncated domain, shown in Figure 1, is only a subset of a surrounding enlarged domain, which includes a seismic source.

Namely, the wave solution in the enlarged domain is employed to obtain data that is highly randomized in terms of (i) the effective seismic forces within a DRM layer of the reduced domain of interest, which are used as the output-layer features and (ii) the ground-surface displacement measurement ($\mathbf{u}^{\text{m}}$) at sensor locations, which are used as the input-layer features.

3.1.1 | Description of site examples

This work considers examples of sites with two different geophysical profiles. For each of the two sites, we generate separate data sets to train two distinct CNNs. Figure 2A shows an enlarge domain, including a reduced domain of a homogeneous material (site profile 1), while Figure 2B shows an enlarge domain in which the reduced domain is occupied by a heterogeneous material (site profile 2). Their geophysical profiles are described in the following.

- **Site profile 1: an enlarged domain including a homogeneous reduced domain (Figure 2A)**: four layers with shear wave velocities V_{s_1} to V_{s_4} of 1800, 1500, 300, and 200 m/s, respectively; and mass density $\rho = 1500$ kg/m^3 for the entire domain.

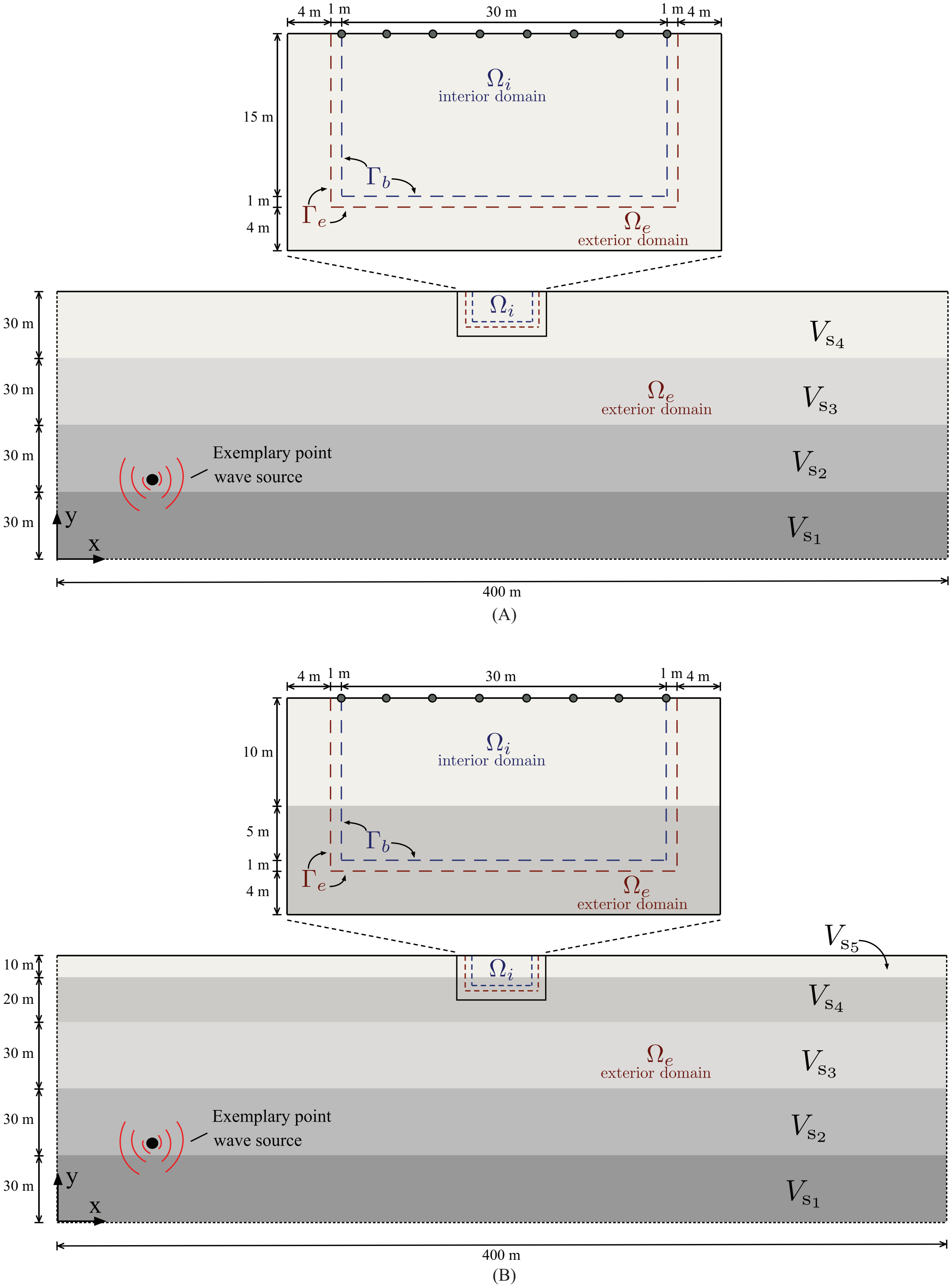

FIGURE 2 Enlarged domains used to generate the randomized input- and output-layer data sets. (A) Enlarged domain comprising a homogeneous reduced domain (site profile 1). (B) Enlarged domain comprising a heterogeneous reduced domain (site profile 2).

- **Site profile 2: an enlarged domain encompassing a heterogeneous reduced domain (Figure 2B)**: five layers with V_{s_1} to V_{s_5} of 1800, 1500, 300, 250, and 200 m/s, respectively; and uniform $\rho = 1500$ kg/m^3.

For both site profiles, the dimensions of the enlarged domains are set to be 400 m × 120 m, and they are subject to the traction-free condition on the top surface, and the WABC on the left, bottom, and right boundaries. On the other hand, the dimensions of the reduced domains are set to be 40 m × 20 m, and they are localized at the top–middle part of the enlarged domains while seismic sources are located outside the truncated domains. Thus, the simulations in the enlarged domains mimic typical realistic scenarios, where a remote seismic source imparts waves that hit a truncated domain of interest. Another key aspect of the wave simulations in the enlarged domains is that we systematically randomize the incident waveforms that impinge the reduced domain. Thus, the corresponding DRM force sets, each of which represents a different incident waveform, will be randomized, and so are corresponding measured wave responses at the sensor locations.

3.1.2 | Methodology to generate each data set via the wave solution from an enlarged domain

On wave simulations in an enlarged domain:
In each data set made during the data generation process, the wave motions in the enlarged domain are generated by point wave sources, which are randomized per each data set and characterized by the following antiplane directional point forces:

$$P(x, y, t) = \sum_{i=1}^{N_p} P_i(x, y, t), \tag{4}$$

$$P_i(x, y, t) = \begin{cases} -A_i^{\text{peak}} \times \dfrac{\left(0.25\eta_i^2 - 0.5\right) e^{-0.25\eta_i^2} - 13e^{-13.5}}{0.5 + 13e^{-13.5}} \times \delta\left(x - x_i^s, y - y_i^s\right), & t \le \bar{t}, \\ 0, & t > \bar{t}, \end{cases} \tag{5}$$

where $P_i(x, y, t)$ is the ith point loading of the Ricker wavelet signal with $\eta_i = \omega_i(t - t_i^p) - 3\sqrt{6}$; $\bar{t} = 6\sqrt{6}/\omega_i$; $\omega_i = 2\pi f_i$. The number of point sources (N_p) and their locations (x_i^s and y_i^s, horizontal and vertical coordinates, respectively), central frequencies (f_i), peak amplitudes (A_i^{peak}), and a timing (t_i^p) from the beginning of the observation duration, at which the ith point source initiates its Ricker force signals, are randomly defined for each ith data set.

The enlarged domains are discretized in a structured mesh[2] by using an element size of 1 m. A total observation duration of 1.5 s and a time step of 0.003 s are utilized for time discretization. The wave simulations in the enlarged domain are performed by using the FEM and the implicit Newmark time integration scheme.

A minimum node density of around 10 nodes per wavelength is necessary for accurate wave propagation in our computational simulations. For the examples provided, we ensure that the number of nodes per the shortest wavelength exceeds the minimum desired density. To be precise, considering the lowest wave speed of 200 m/s (i.e., V_{s_4} of site profile 1 and V_{s_5} of site profile 2) and the highest discernible frequency of 15 Hz, the shortest wavelength measures about 13 m. As mentioned before, the space discretization is 1 m, resulting in 13 nodes per the shortest wavelength. Therefore, increasing the mesh size may lower the computational cost for both wave simulations during data generation and CNN training. Nevertheless, this may lead to a decrease in CNN accuracy for high-frequency waves.

On the extraction of labeled data:
In each data set, the input and output–layer feature data are calculated using the solution of the wave problem in an enlarged domain as follows.

- **Input-layer features**: The measured displacement fields of wave motions ($\mathbf{u}^{\text{m}}$) at the sensors (i.e., the input-layer features) are extracted from the wave solution computed in the enlarged domain. To this end, 31 sensors are located on the surface of the reduced domain with a 1 m spacing from each other.
- **Output-layer features**: The corresponding DRM forces will be calculated, as the output-layer features, by using the wave solution from the enlarged domain. Due to the space discretization in the reduced domain Ω, there are 61 and 65

---

[2] While the present method can be applied to an unstructured mesh, we chose to use a structured mesh for ease of implementation.

ALGORITHM 1 Randomizer to generate data sets.

```
Choose between a homogeneous or heterogeneous reduced domain (site profiles 1 or 2).
Build mass, stiffness, and damping matrices for the respective enlarged domain setting.
for iteration ← 1 to (total number of iterations = 20,000) do
    Randomly choose the number of point wave sources ($N_p$): between 1 or 2.
    for point wave source index $i \leftarrow 1$ to ($N_p$) do
        $0 \leq t_i^p \leq 0.05$ s,
        $50 \leq A_i^{\text{peak}} \leq 150$ N/m$^2$,
        $1 \leq f_i \leq 5$ Hz,
        $20 \leq y_i^s \leq 110$ m,
        if $y_i^s > 90$ then
            $50 \leq x_i^s \leq 160$ m
        else
            $50 \leq x_i^s \leq 200$ m
        end if
    end for
    Solve the 2D wave propagation problem in an enlarged domain.
    Save the displacement data at every time step from sensor locations on the surface as input-layer features.
    Save the effective nodal forces on $\Gamma_b \cup \Gamma_e$ at every time step as output-layer features.
end for
```

discrete nodes along Γ_b and Γ_e, respectively. Thus, per the DRM theory, a total of 126 discrete nodes are subject to nodal DRM forces. For computing the nodal forces on Γ_e and Γ_b, the DRM theory is used with incident waves $\mathbf{u}^0$ that impinge the reduced domain (i.e., the wave motions in the enlarged domain that pass through the reduced domain). Namely, $\mathbf{F}$ in Equation (3) at any discrete time step t can be computed using the incident motions as follows (for details, please refer to Bielak et al.[23]):

$$\mathbf{F}(t) = \begin{bmatrix} \mathbf{0} \\ \mathbf{P}_b^{\text{eff}}(t) \\ \mathbf{P}_e^{\text{eff}}(t) \end{bmatrix} = \begin{bmatrix} \mathbf{0} \\ -\mathbf{K}_{be}^{\Omega_e}\mathbf{u}_e^0(t) - \mathbf{M}_{be}^{\Omega_e}\ddot{\mathbf{u}}_e^0(t) \\ \mathbf{K}_{eb}^{\Omega_e}\mathbf{u}_b^0(t) + \mathbf{M}_{eb}^{\Omega_e}\ddot{\mathbf{u}}_b^0(t) \end{bmatrix}, \tag{6}$$

where subscripts b and e identify the nodes in Γ_b and an exterior domain Ω_e, respectively. Specifically, $\mathbf{u}_b^0$ and $\mathbf{u}_e^0$ indicate the subsets of the vectors of incident motions $\mathbf{u}^0$ at the discrete time step t on Γ_b and in Ω_e. $\mathbf{K}_{be}^{\Omega_e}$, $\mathbf{K}_{eb}^{\Omega_e}$, $\mathbf{M}_{be}^{\Omega_e}$, and $\mathbf{M}_{eb}^{\Omega_e}$ are the subsets of the global stiffness and mass matrices (mentioned in Equation (3)), for the reduced domain, of which row and column indices correspond to the nodes on Γ_b and in Ω_e. Please note that all the components of $\mathbf{P}_b^{\text{eff}}(t)$ occupies all the nodes on Γ_b, and $\mathbf{P}_e^{\text{eff}}(t)$ has nonzero values only at Γ_e. The rest of $\mathbf{P}_e^{\text{eff}}(t)$ are zero and correspond to the nodes in Ω_e except for Γ_e. Thus, the output-layer feature data (the DRM forces) consists of all the components of $\mathbf{P}_b^{\text{eff}}(t)$ and the specific components of $\mathbf{P}_e^{\text{eff}}(t)$ that are located only on Γ_e at all the discrete time steps during the observation period.

We train a total of two CNNs, each of which considers Example 1 or 2. In each example, the randomizer is configured to perform 20,000 iterations, producing training, validation, and test data sets. At each iteration of our randomizer, we (i) extract the displacement $\mathbf{u}^{\text{m}}$ from 31 sensors for every time step and (ii) calculate the DRM forces at the 126 nodes on $\Gamma_b \cup \Gamma_e$ for all the time steps by using the wave solution from the enlarged domain solver. Algorithm 1 shows a pseudo code, showing the structure of our randomizer. Please also see Figure 3 for the overall flowchart of the data-generating simulation using the enlarged domain wave solver.

We note that a typical running time for one iteration of the data generation using the enlarged model, with random seismic sources, is 26 s in a modern workstation using a single CPU of 3.5 GHz. Furthermore, generating tens of thousands of training data is not uncommon in the area of supervised learning for the inverse problems involving a large size of input

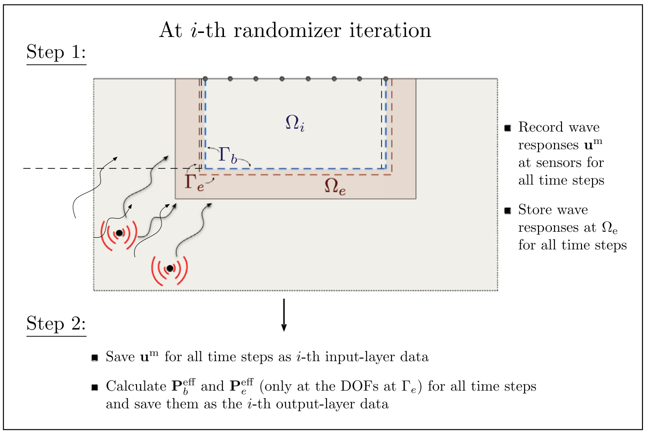

- Record wave responses $\mathbf{u}^{\mathrm{m}}$ at sensors for all time steps
- Store wave responses at Ω_e for all time steps

- Save $\mathbf{u}^{\mathrm{m}}$ for all time steps as i-th input-layer data
- Calculate $\mathbf{P}_b^{\mathrm{eff}}$ and $\mathbf{P}_e^{\mathrm{eff}}$ (only at the DOFs at Γ_e) for all time steps and save them as the i-th output-layer data

FIGURE 3 Flowchart of the data generation procedure using the enlarged domain wave solver.

feature (e.g., 501 time steps × 31 sensors, totaling 15,531 discrete data points) and a large size of output feature (e.g., 501 time steps × 126 DRM nodes, totaling 63,126 discrete data points).

3.2 | Data preparation

The present study employs a preprocessing technique on a generated data set comprising 20,000 samples, which are subsequently divided into subsets for training, validation, and testing purposes. The duration covered by each sample spans 500 discrete timesteps for the total observation duration of 1.5 s, corresponding to a temporal resolution of 0.003 s. Consequently, the input data matrix is characterized by a dimensionality of 31 sensors multiplied by 500 timesteps. Furthermore, the output data matrix consists of 500 discrete timesteps with DRM force values located on 126 nodal locations within a DRM layer.

The computational infrastructure employed for training a neural network on the aforementioned data set comprises a high-performance system configuration. Specifically, the training computations were performed on a robust system comprising a 24-core central processing unit (CPU) endowed with 256 gigabytes of DDR4 random-access memory (RAM), along with 512 gigabytes memory NVIDIA Tesla V100 graphics processing unit (GPU). Notably, the data set was partitioned in a stratified manner, reserving 80% (16,000 samples) for training, while allocating 10% (2000 samples) to the validation set and the remaining 10% (2000 samples) to the testing set.

Figure 4A exhibits a representative sample of the input-layer feature data from a randomly chosen single sensor, while Figure 4C showcases a sample of the output-layer feature data obtained at a randomly chosen single node in a DRM layer. Figure 4A reveals that the measurement data $\mathbf{u}^{\mathrm{m}}$ encompasses magnitudes spanning a range of -10^{-7} to 10^{-7}. Moreover, Figure 4C shows a sample DRM force at one node within a DRM layer, and its scale is predominantly in the double-digit range. The significant disparity in range of values between the input and output data poses challenges for the neural network to effectively discern meaningful relationships among features. In order to address this concern and enable the efficient acquisition of feature relationships between the input and output layers within our CNN, we employ a normalization technique by utilizing the following Equation (7).

$$A_{ijk}^{n} = \frac{A_{ijk} - A_{\text{train}}^{\text{mean}}}{A_{\text{train}}^{\text{max}} - A_{\text{train}}^{\text{min}}}, \tag{7}$$

In the equation above, A_{ijk}^{n} represents the normalized element of a data matrix, which may represent the training, validation, or test set. The jth row and kth column correspond to the kth time-step of the jth sensor value out of 31 sensors (or the jth nodal numbering out of 126 DRM nodes) pertaining to the ith data set. A_{ijk} denotes the corresponding unnormalized component of the data matrix. $A_{\text{train}}^{\text{mean}}$ represents the mean value of the training data set matrix. $A_{\text{train}}^{\text{max}}$ and $A_{\text{train}}^{\text{min}}$ represent the maximum and minimum values of the training data set matrix, respectively. These mean, maximum, and minimum values are necessary for de-normalizing the predicted data obtained from CNN.

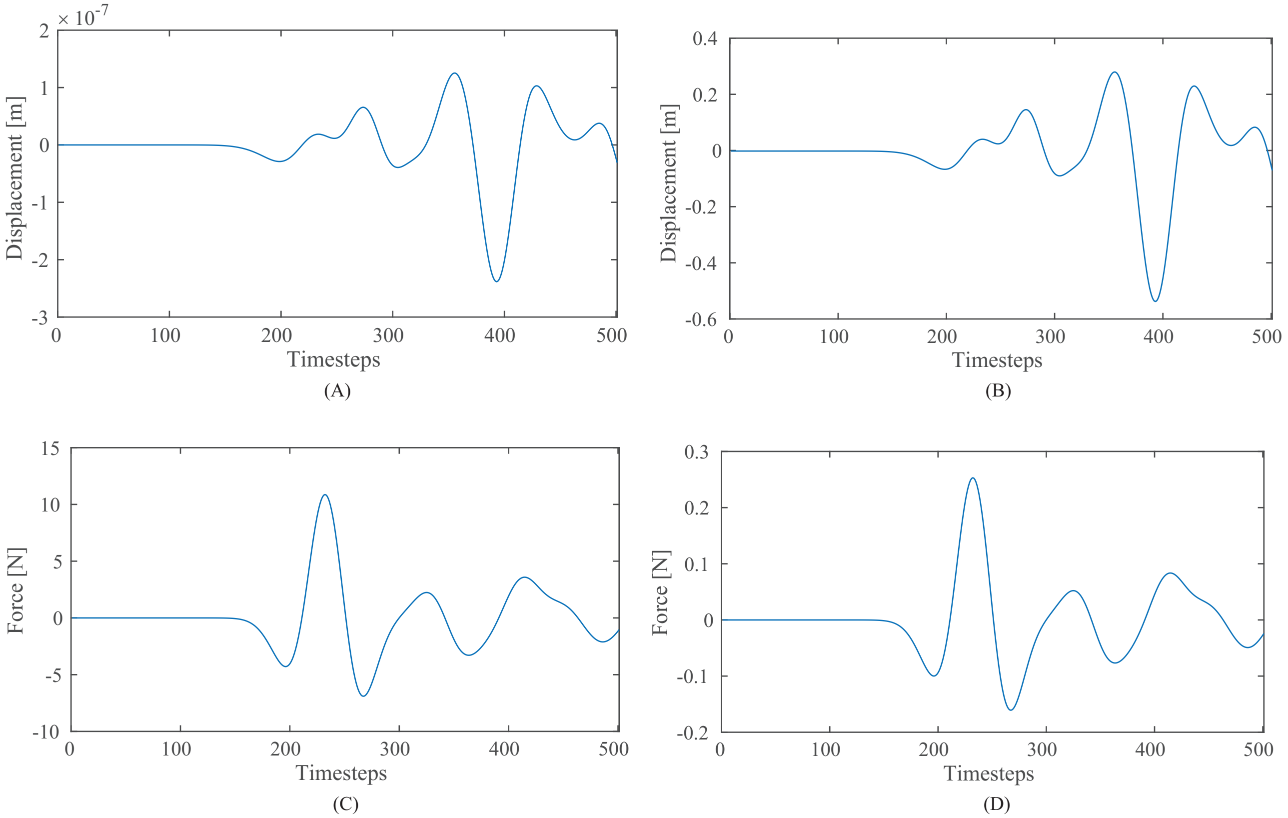

FIGURE 4 A sample of input-layer measured response and output-layer DRM force waveforms. (A) Displacement waveform before normalization. (B) Displacement waveform after normalization. (C) DRM Force waveform before normalization. (D) DRM Force waveform after normalization.

Figure 4B uses the normalized scales of sample input-layer feature data, which range in values between −0.5 and 0.5, as shown on the vertical axes. Figure 4D shows the sample output-layer feature data that are normalized. The waveform shape remains unaltered as a result of the linear normalization process. Subsequently, the normalized data are fed into the CNN to establish a data-informed framework for DRM-force identification, utilizing the input displacement data.

3.3 | Evaluation metrics

To assess the efficacy and predictive capabilities of our neural network model, we employed well-established evaluation metrics, namely the mean-absolute error (MAE) and mean-squared error (MSE) in Equations (8b) and (8a), in addition to our customized error functions ($\mathcal{E}$ and $\mathcal{E}^u$) formulated in Equations (9a) and (9b). The incorporation of this custom error function was purposeful, aiming to provide a supplementary metric for evaluating the performance of our CNN predictions. Furthermore, this enhancement enables a comparative analysis of our DRM-force reconstruction with the benchmark solutions from a time-consuming PDE-constrained optimization-based DRM-force inversion method previously presented by Guidio et al.[22]

$$\text{MSE} = \frac{1}{n} \sum_{i=1}^{n} \sum_{j=1}^{l} \sum_{k=1}^{m} \left(F_{ijk}^{\text{recon.}} - F_{ijk}^{\text{tar.}} \right)^2, \tag{8a}$$

$$\text{MAE} = \frac{1}{n} \sum_{i=1}^{n} \sum_{j=1}^{l} \sum_{k=1}^{m} \left| F_{ijk}^{\text{recon.}} - F_{ijk}^{\text{tar.}} \right|, \tag{8b}$$

where n is the number of data sets; l is the number of nodes in a DRM layer; m is the count of time step features of data; $F_{ijk}^{\text{tar.}}$ is the i-th record at the j-th DRM node and k-th time step feature of the targeted output-layer data; and $F_{ijk}^{\text{recon.}}$ is the corresponding output-layer data associated with the CNN prediction.

For each i-th test data set, we also evaluate the error ($\mathcal{E}$) between the targeted DRM forces and the inverted counterparts, as well as that ($\mathcal{E}^u$) between the targeted wave responses in the domain and the reconstructed counterparts induced by the identified DRM forces as:

$$\mathcal{E}_i = \frac{\sum_{j=1}^{l}\sum_{k=1}^{m}\left|F_{ijk}^{\text{recon.}} - F_{ijk}^{\text{tar.}}\right|^2}{\sum_{j=1}^{l}\sum_{k=1}^{m}\left|F_{ijk}^{\text{tar}}\right|^2} \tag{9a}$$

$$\mathcal{E}_i^u = \frac{\sum_{j=1}^{q}\sum_{k=1}^{m}\left|u_{ijk}^{\text{recon.}} - u_{ijk}^{\text{tar.}}\right|^2}{\sum_{j=1}^{q}\sum_{k=1}^{m}\left|u_{ijk}^{\text{tar.}}\right|^2} \tag{9b}$$

where q denotes the number of the nodes within Ω_i (i.e., 496 nodes due to the space discretization), at which the wave responses are computed per either targeted DRM forces or identified ones.

3.4 | Hyperparameter search and optimization

In order to streamline the laborious and time-consuming process of hyperparameter search, we implemented custom algorithms to automate it. Through extensive experimentation, we explored various combinations of layers and learnable parameters. We then fine-tuned the most promising combination manually to achieve optimal results on the validation data. As a result, our showcased CNN model is highly optimized and delivers robust results when applied to the test data set. Furthermore, callback methods provided by TensorFlow were utilized to monitor the learning progress during training, and when the model's performance on validation data showed no further improvement for 5 iterations (i.e., epochs), the callback was triggered to halt the training process early. This prevented overfitting effectively by stopping the process from running beyond the necessary epoch. Finally, in order to accomplish the process of hyperparameter optimization following the search, we leverage TensorFlow's provided backpropagation and the automated differentiation algorithm.

4 | EXAMPLE 1: A TRUNCATED DOMAIN WITH A HOMOGENEOUS SOIL (SITE PROFILE 1)

This section presents the CNN architecture designed to identify DRM forces in a homogeneous reduced domain based on surface measurement data. It also includes an analysis of the CNN's performance on the test data set.

4.1 | CNN architecture

We adopt a CNN architecture, which can be manipulated to reduce computational intensity while retaining the essential spatial and temporal structure of the data. Moreover, due to the high computational demands of fully-connected dense networks, we made a deliberate decision not to use them. Instead, we chose to employ a convolutional layer throughout the final output layer.

We present our approach to process the input data with dimensions of 500 × 31 using a CNN. The initial step involves passing the input data through our first convolutional layer, wherein the convolutional operation employs a sliding dot product mechanism,[43] as illustrated in Figure 5. This layer comprises 480 filters, each possessing a filter size of 80. To enhance training stability and acceleration, a batch normalization layer is applied to the output of the first convolutional layer. This layer normalizes the input data within each mini-batch during the training process. Subsequently, the resulting feature map is forwarded to another convolutional layer, which comprises 512 filters of size 80, followed by another batch normalization layer. The feature representation of the input data is further refined through the subsequent processing and is then forwarded to the final output convolutional layer. For this final layer, we deliberately opted to use 126 filters, each with a size of 90. This choice was motivated by the need to accurately reconstruct the 126 nodal DRM force values in the output layer. We employed the "Leaky ReLU" activation function for all layers containing learnable parameters. This

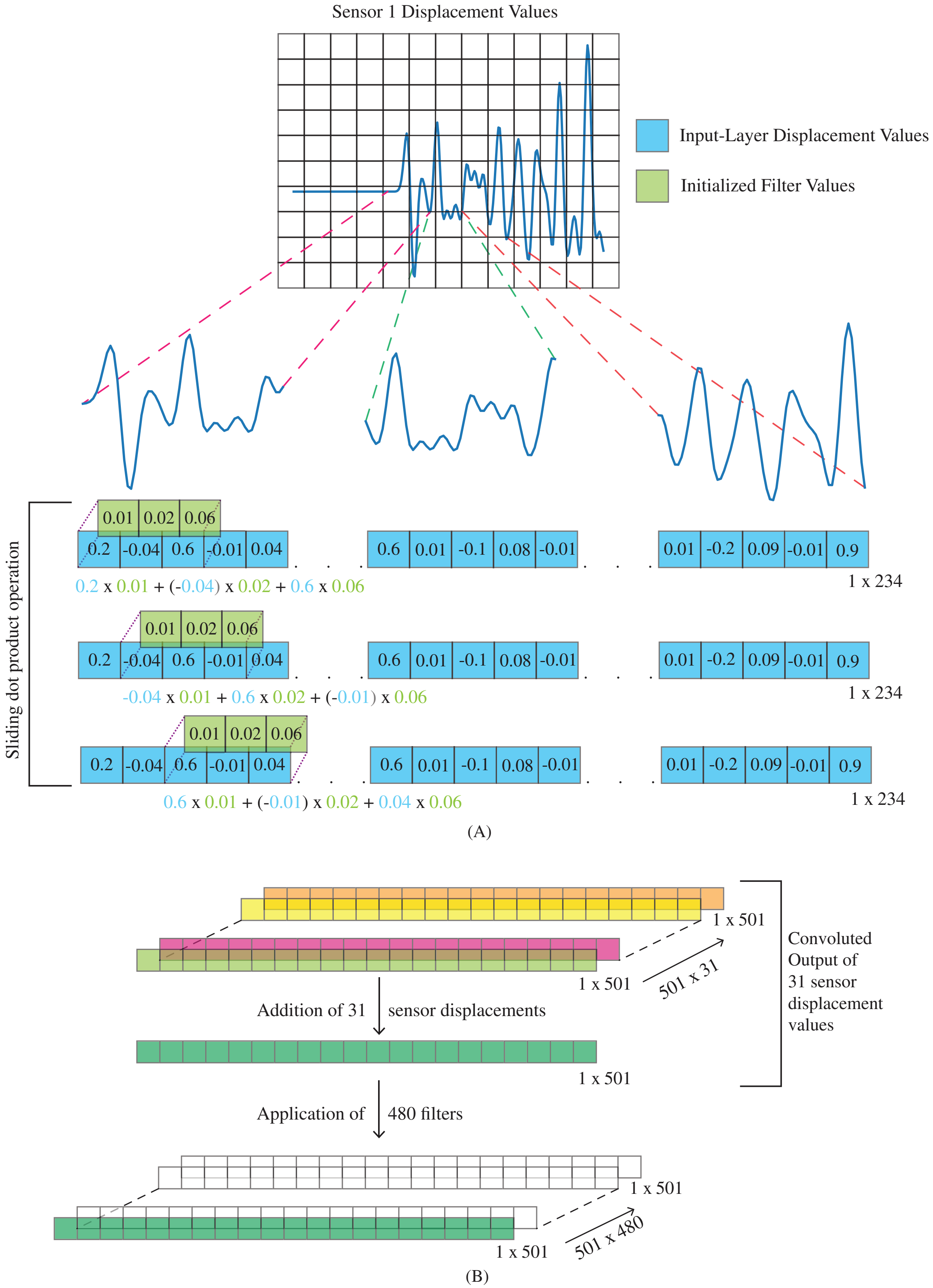

FIGURE 5 Sliding dot product application of a 1D CNN filter operation. (A) Application of a single 1D CNN filter on one sensor displacement value. (B) Application of 480 1D CNN filters across 31 sensor displacement values.

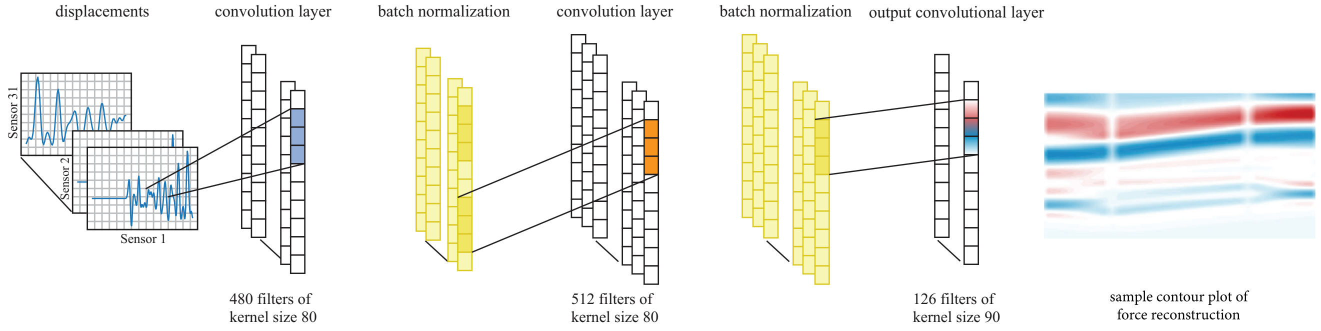

FIGURE 6 Our CNN designed for reconstructing DRM forces in Example 1.

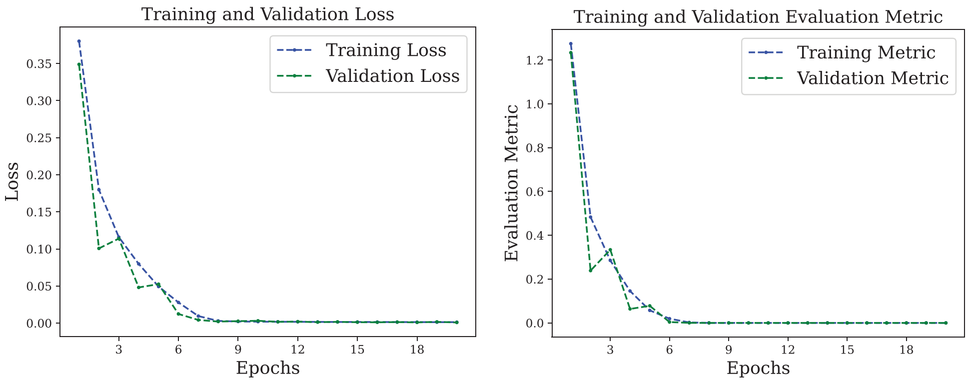

(A) (B)

FIGURE 7 Convergence of loss function and evaluation metrics across 20 epochs in Example 1. (A) Mean-absolute error (MAE). (B) Mean-squared error (MSE).

choice was made to facilitate the introduction of non-linear learning capabilities, enabling the model to effectively capture and understand intricate feature relationships between the input- and output-layer data across the network's architecture. Our CNN architecture for Example 1 is shown in Figure 6.

During our training process, we employ two evaluation metrics: MAE for computing the loss function's value over the epochs, and MSE to evaluate the model's performance. To optimize the neural network, we use the "Adamax" optimizer with a learning rate of 0.001, and the training was set to run for a maximum of 25 epochs. As mentioned in Section 3.4, we utilize a callback function that would stop the training if the model's validation data set performance did not improve for 5 consecutive epochs. As a result, the neural network trained for a total of 20 epochs, leading to optimized hyperparameters that yields excellent DRM force reconstruction results.

4.2 | Numerical experiments

4.2.1 | Performance during training

We present the results of our CNN as it undergoes training and simultaneously evaluates its behavior on the validation data set. These results are shown in Figure 7. Both Figures 7A and 7B illustrate a clear trend where the loss (MAE) and evaluation metric (MSE) steadily decrease over the epochs during training. Eventually, they reach a minimum and remain consistently low, indicating that the chosen hyperparameters are well-suited for the task.

4.2.2 | Performance of the trained CNN on test data set

We use our optimized CNN to make predictions on a test data set consisting of 2000 samples. The outcomes of our predictions are summarized quantitatively in Table 1 and visualized at the histogram in Figure 8. To comprehensively

TABLE 1 Table listing the five force and response reconstruction error ($\mathcal{E}$ and $\mathcal{E}^u$, respectively) statistics in percentage in Example 1.

	Reconstruction error	
Test data set	**Force ($\mathcal{E}$)**	**Wave response ($\mathcal{E}^u$)**
Lowest error (Figures 9 and 10)	0.73%	0.69%
25th percentile	1.71%	1.56%
50th percentile (Figures 11 and 12)	2.01%	1.58%
75th percentile	2.28%	2.51%
Highest error (Figures 13 and 14)	35.32%	18.86%

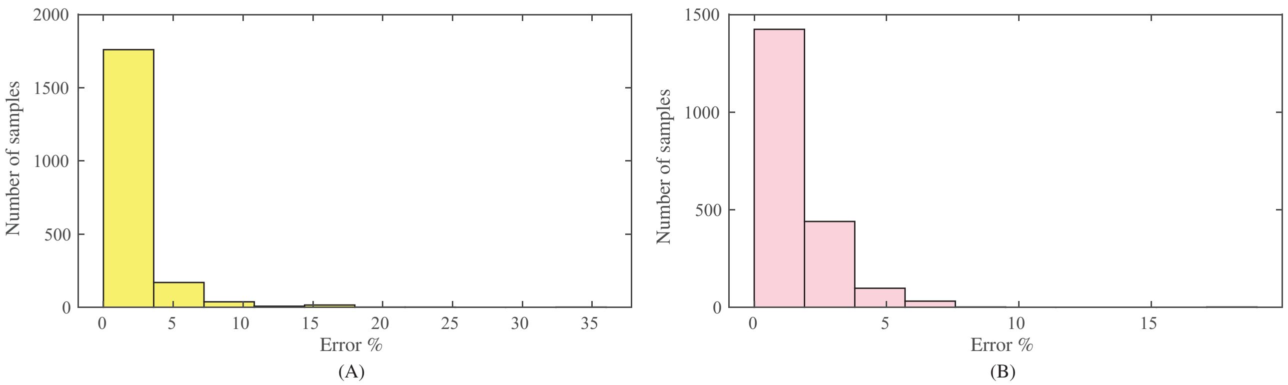

FIGURE 8 Reconstruction error ($\mathcal{E}$ and $\mathcal{E}^u$) distribution across the 2000 test data set in Example 1. (A) $\mathcal{E}$ for DRM force identification. (B) $\mathcal{E}^u$ for wave response reconstruction.

demonstrate the distribution of these predictions, we employed five statistical metrics in terms of the value of the error $\mathcal{E}$: the minimal error $\mathcal{E}$ (the best performance), the 25th percentile, the 50th percentile (the median), the 75th percentile, and the maximum $\mathcal{E}$ (the poorest performance).

For the DRM-force identification task, our CNN achieved remarkably low-valued errors of $\mathcal{E}$ for the most of the test data sets. Specifically, for the best performance in terms of $\mathcal{E}$, we obtained an impressive error $\mathcal{E}$ of the minimal value of 0.73% (Figure 9) for the DRM force identification and an equally remarkable 0.69% error $\mathcal{E}^u$ (Figure 10) for the wave response reconstruction based on the identified DRM force. In the 25th percentile case of $\mathcal{E}$, the identified DRM force yielded an error $\mathcal{E}$ of 1.71%, which translated to an accurate wave response reconstruction with $\mathcal{E}^u$ of 1.56%. At the 50th percentile, $\mathcal{E}$ slightly increased to 2.01% (Figure 11), still maintaining a favorable $\mathcal{E}^u$ of 1.58% (Figure 12). Upon reaching the 75th percentile, we observed a marginally higher $\mathcal{E}$ of 2.28% for the DRM force identification, leading to $\mathcal{E}^u$ of 2.51%. Lastly, the highest $\mathcal{E}$ we encountered was 35.32% (Figure 13), resulting in a substantial value of $\mathcal{E}^u$ of 18.86% (Figure 14). Additionally, it was observed that over 92% of the test data set falls under the $\mathcal{E}$ threshold of 5%, and further 98% falls under the 10% for $\mathcal{E}$. It was noted that nearly 97% of the test data falls under the 5% $\mathcal{E}^u$ threshold, and over 99% of the test data falls under the 10% $\mathcal{E}^u$ threshold. Overall, the numerical and graphical results for Example 1 are exceptionally promising.

5 | EXAMPLE 2: A TRUNCATED DOMAIN WITH A HETEROGENEOUS SOIL (SITE PROFILE 2)

5.1 | CNN architecture

We utilize a similar approach to the previous CNN architecture of Example 1 for this presented Example 2 using only convolutional layers to learn important feature relationships between the input- and output-layer data. Due to the complex nature of Example 2 involving the heterogeneous profile, we added another convolutional layer, resulting in three blocks of convolutional operation as shown in Figure 15. We feed the input data to the first convolutional layer consisting of 512 filters and a kernel size of 40. Like previously, we batch-normalize this data to stabilize and accelerate the training processes. The subsequent convolutional block consists of 352 filters of 50 kernel size. In addition, the penultimate layer

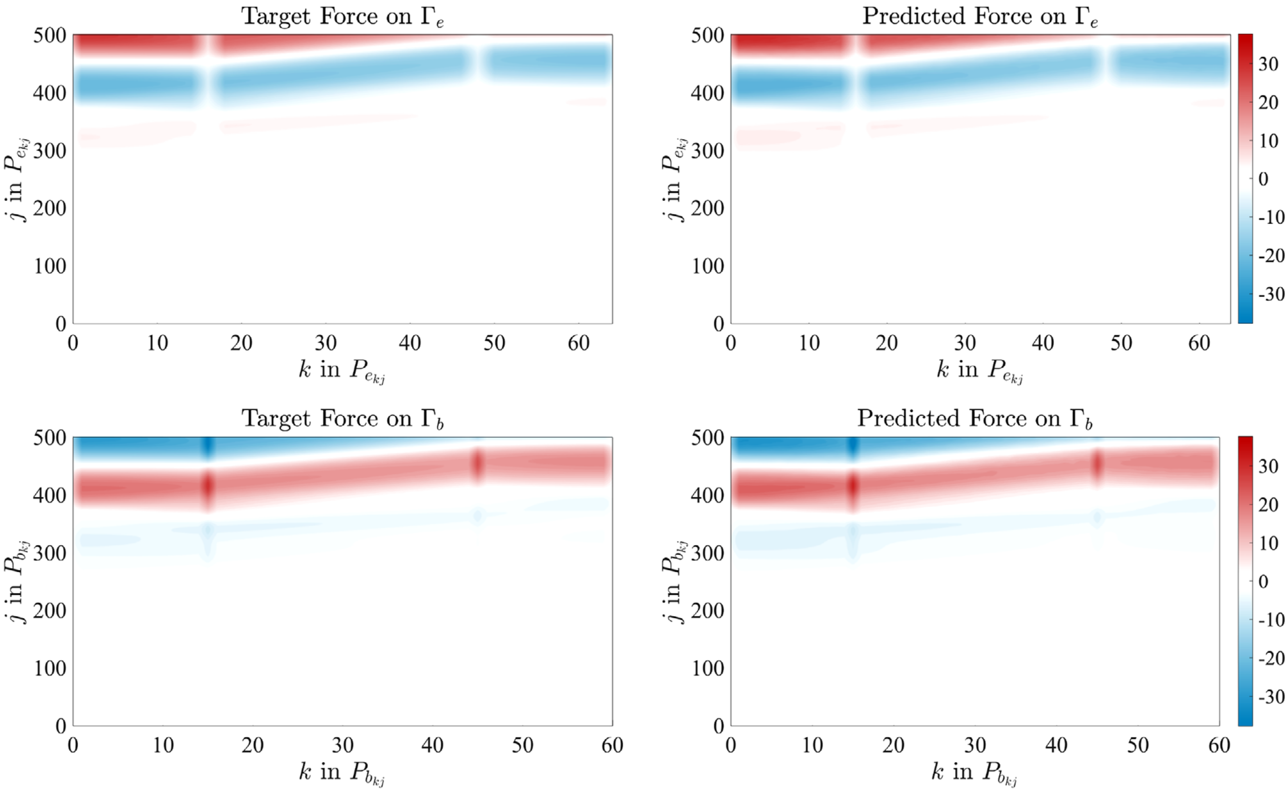

FIGURE 9 DRM force identification using our CNN in Example 1 (the best case of $\mathcal{E}$ of 0.73%).

of our neural network consists of another convolutional block consisting of 40 filters and a filter size of 40. The feature extracted convoluted data are then passed to the final output convolutional layer to produce a result mimicking the target DRM force. To compile the model, we utilize MAE as the loss function and MSE as the evaluation metric. To optimize the model, we chose the "Adamax" optimizer with a learning rate of 0.001. Similar to Example 1, we utilize a convenient TensorFlow provided with the callback function, which led to the full optimization of our CNN architecture in 18 iterations.

5.2 | Numerical experiments

5.2.1 | Performance during training

As outlined in Section 4.2.1, we demonstrate the convergence of MAE and MSE values during training, as depicted in Figure 16. The metrics on the validation data set follow a similar pattern and converge towards a minimum value, mirroring the training metrics' behavior. This convergence further leads to the obtaining of highly optimized hyperparameters, resulting in excellent predictive performance.

5.2.2 | Performance of the trained CNN on test data set

Similar to Example 1, our CNN demonstrates exceptional performance in the DRM force identification, achieving remarkably low errors. The results are summarized in Table 2 and Figure 17. Specifically, the lowest error rate for the DRM force identification was an impressive error $\mathcal{E}$ 0.22% (Figure 18), and for wave response based on the identified DRM force, it was equally remarkable error $\mathcal{E}^u$ at 0.20% (Figure 19). Even at the 25th percentile in terms of $\mathcal{E}$, the error $\mathcal{E}$ remained low at 1.02%, corresponding to a highly accurate wave response reconstruction error $\mathcal{E}^u$ of 1.77%. Moving to the 50th percentile in term of $\mathcal{E}$, the DRM force identification error $\mathcal{E}$ slightly increased to 1.12% (Figure 20), while still maintaining a favorable wave response reconstruction error $\mathcal{E}^u$ of 0.82% (Figure 21). As we reached the 75th percentile, a marginally higher error $\mathcal{E}$ of 1.93% was observed for the DRM force identification, leading to a wave response discrepancy $\mathcal{E}^u$ of 1.40%. The most

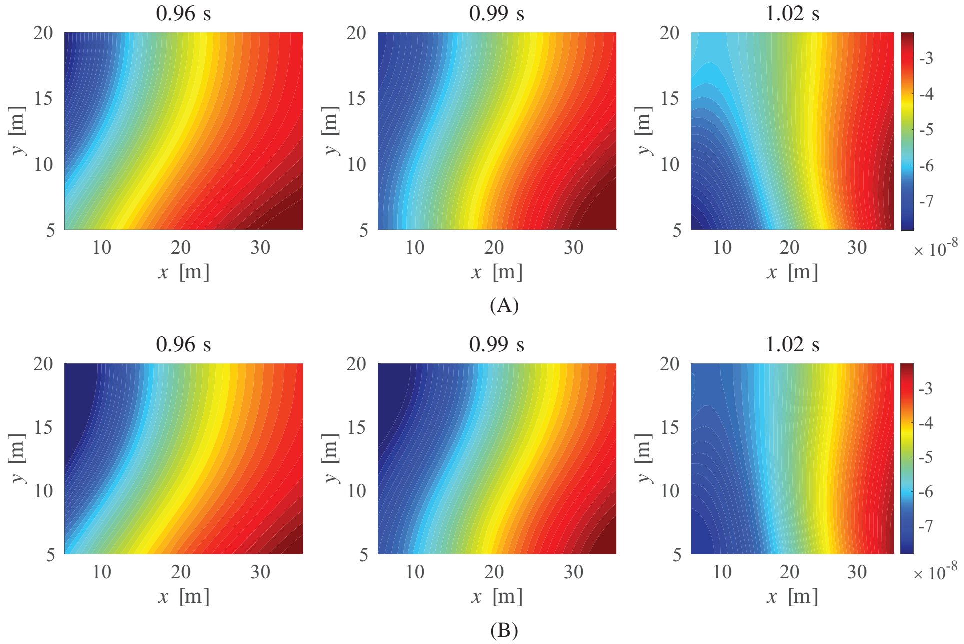

FIGURE 10 Wave response (u) reconstruction using the identified DRM force shown in Figure 9 in Example 1 shown at three distinct timesteps (the best case of $\mathcal{E}^u$ of 0.69%). (A) Target response. (B) Predicted response.

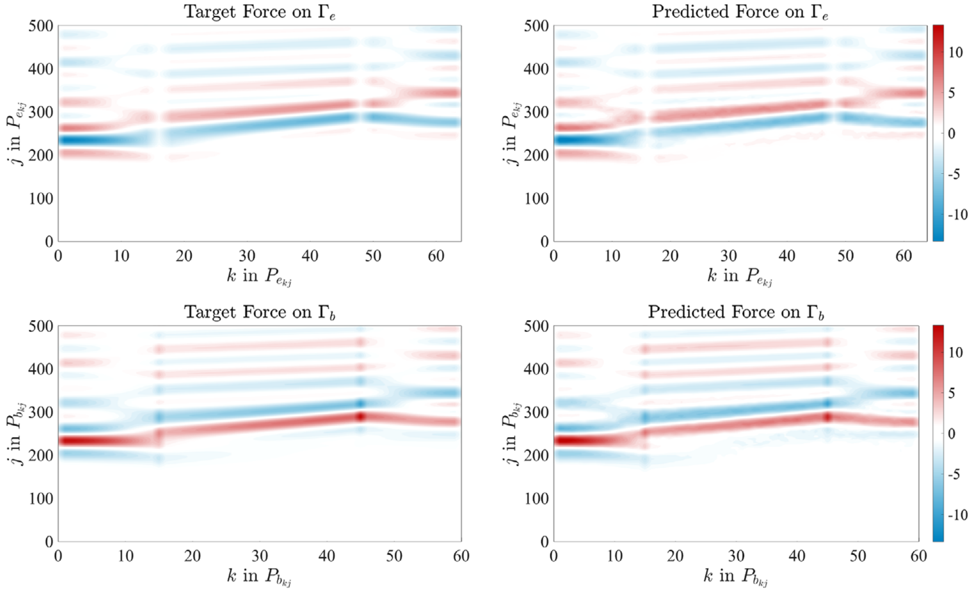

FIGURE 11 DRM force identification at the 50th percentile using our CNN in Example 1 ($\mathcal{E}$ of 2.01%).

TABLE 2 Table listing the five force and response reconstruction error ($\mathcal{E}$ and $\mathcal{E}^u$, respectively) statistics in percentage in Example 2.

	Reconstruction error	
Data set	**Force error ($\mathcal{E}$)**	**Response error ($\mathcal{E}^u$)**
Lowest error (Figures 18 and 19)	0.22%	0.20%
25th percentile	1.02%	1.77%
50th percentile (Figures 20 and 21)	1.12%	0.82%
75th percentile	1.93%	1.40%
Highest error (Figures 22 and 23)	24.52%	29.79%

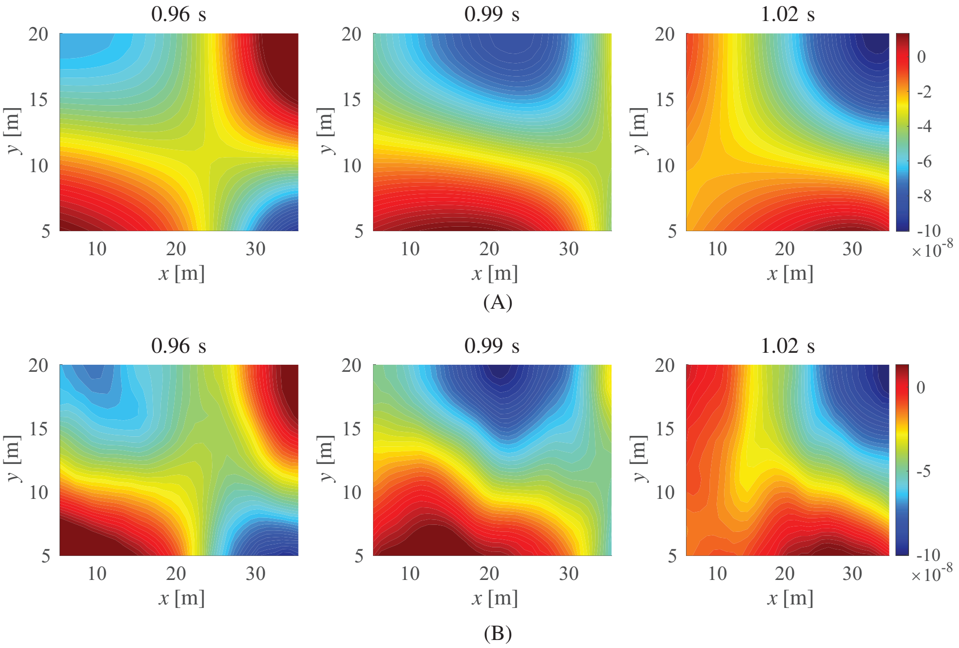

(A)

(B)

FIGURE 12 Wave response (u) reconstruction using the identified DRM force shown in Figure 11 (the 50th percentile) in Example 1 at three distinct timesteps ($\mathcal{E}^u$ of 1.58%). (A) Target response. (B) Predicted response.

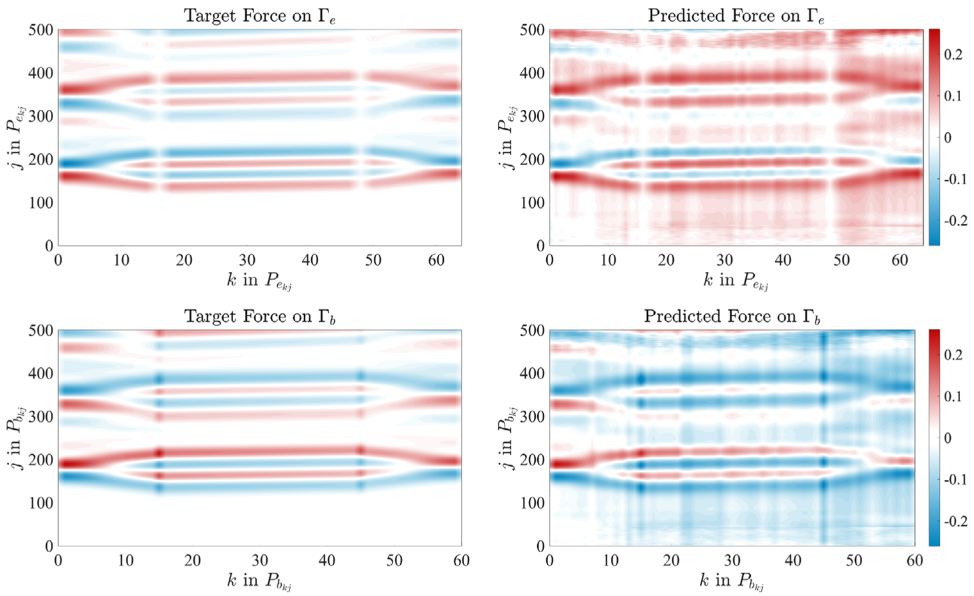

FIGURE 13 The poorest DRM force identification using our CNN in Example 1 ($\mathcal{E}$ of 35.32%).

significant error $\mathcal{E}$ encountered was 24.52% (Figure 22), which resulted in a substantial 29.79% error $\mathcal{E}^u$ in wave response reconstruction (Figure 23). However, it is worth noting that our overall analysis shows that over 95% of the test data set fell within the threshold $\mathcal{E}$ of 5% error, and over 99% remained under $\mathcal{E}$ of 10%. It was observed that nearly 86% of the test data lies within the set for the $\mathcal{E}^u$ threshold of 5%, while over 94% of the test data falls below the 10% threshold of $\mathcal{E}^u$.

5.3 | Example 3: Parametric studies

In this section, we present numerical parametric tests to examine the variations of the CNNs that we train for site profiles 1 and 2 with respect to the number of sensors and the number training data.

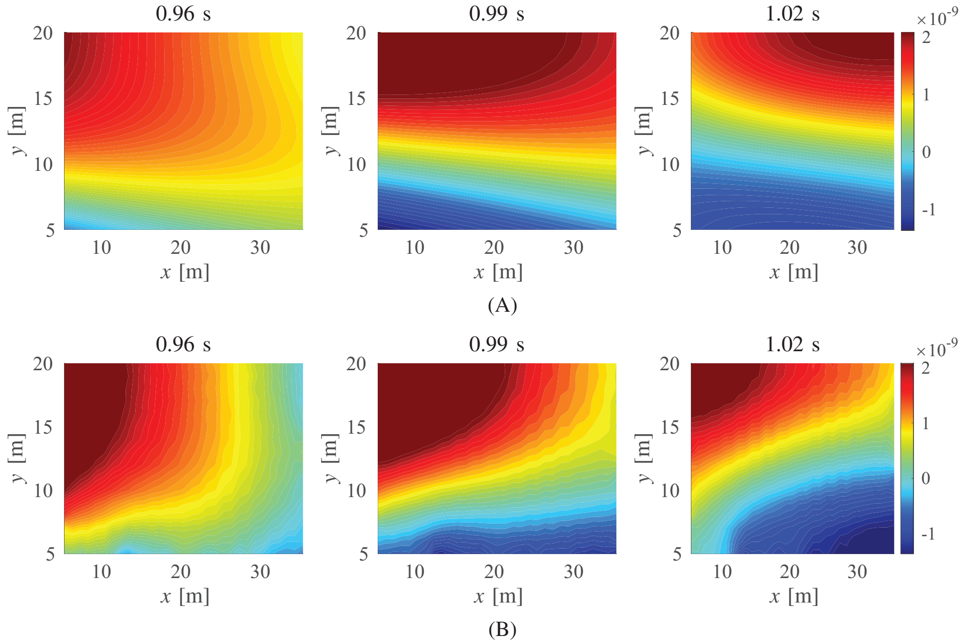

FIGURE 14 Wave response (u) reconstruction using the identified DRM force shown in Figure 13 (the highest error) in Example 1 shown at three distinct timesteps ($\mathcal{E}^u$ of 18.86%). (A) Target response. (B) Predicted response.

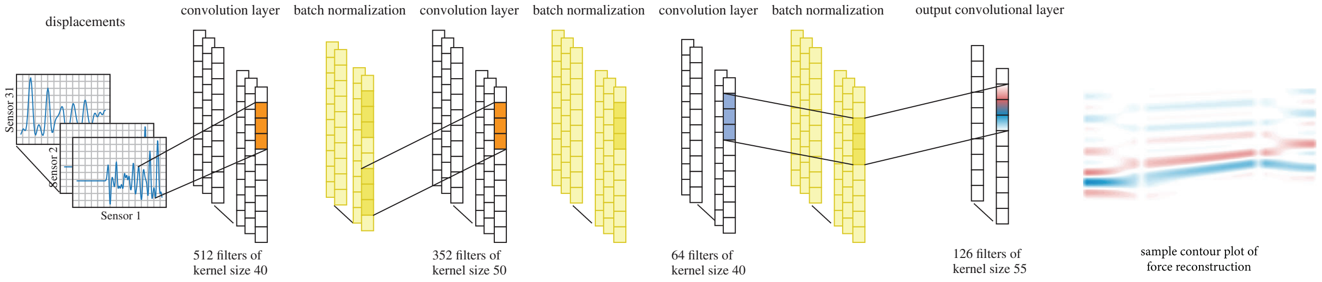

FIGURE 15 Our CNN designed for reconstructing the DRM forces in Example 2.

5.3.1 | Performance of the CNN with respect to the number of sensors

We assess the inversion performance of the presented CNN approach in relation to the number of sensors used in the input-layer features. Specifically, in Examples 1 and 2, we considered 31 sensors spaced 1 m apart on the surface of the reduced domain to extract the measured displacement fields of wave motions. In contrast, we now employ 5, 10, and 15 sensors and compare the inversion accuracy against the results obtained using 31 sensors. The results for the truncated domains, with homogeneous and heterogeneous soils (i.e., site profiles 1 and 2, respectively), are presented in Figure 24.

In Figures 24A and 24B (also in Figures 25A and 25B in Section 5.3.2), we utilize box-and-whisker plots as a concise means to present an overview of our error distributions, with a focus on key statistical parameters. These parameters include the first quartile (25th percentile), the median (50th percentile), the third quartile (75th percentile), the interquartile range (IQR), the minimum and maximum, and the outliers. Each box in the plot spans from the first quartile to the third quartile. Inside this box, a horizontal line signifies the median. The IQR is calculated as the difference between the third quartile and the first quartile, encompassing the middle 50% of the test data. A distance equivalent to 1.5 times the IQR is calculated, and a whisker extends to the furthest data point within this range, both above and below the box. The top end of the upper whisker represents the maximum data point. Conversely, a distance equal to 1.5 times the IQR is measured below the lower quartile (Q1), and a whisker is drawn to the lowest data point within this range. The lower end of the lower whisker represents the minimum data point. These whisker

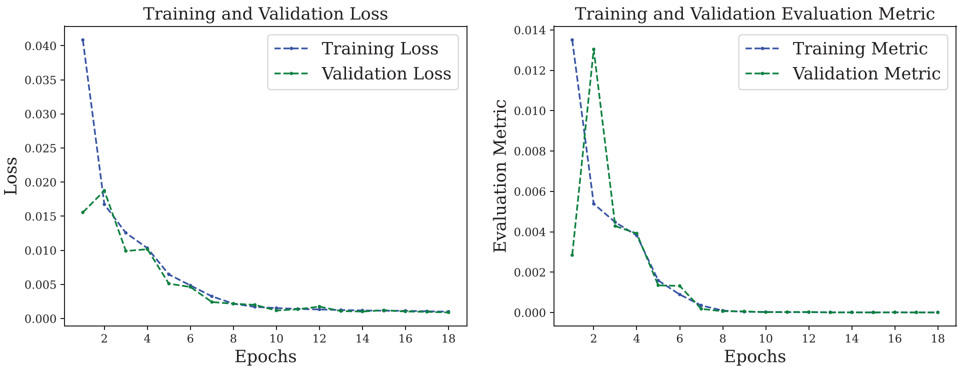

(A) (B)

FIGURE 16 Convergence of loss function and evaluation metrics across 18 epochs in Example 2. (A) Mean absolute error. (B) Mean-squared error.

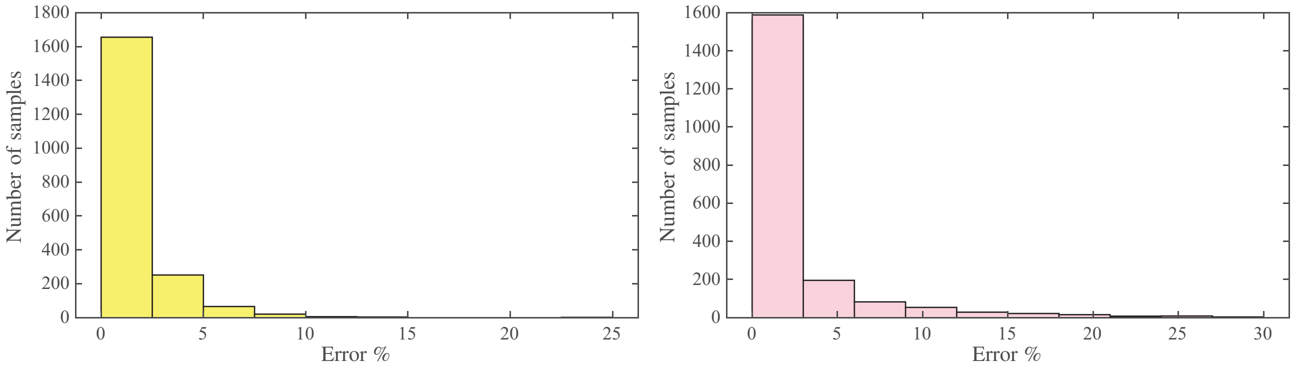

(A) (B)

FIGURE 17 Reconstruction error ($\mathcal{E}$ and $\mathcal{E}^u$) distribution across the 2000 test data set in Example 2. (A) $\mathcal{E}$ for DRM force identification. (B) $\mathcal{E}^u$ for wave response reconstruction.

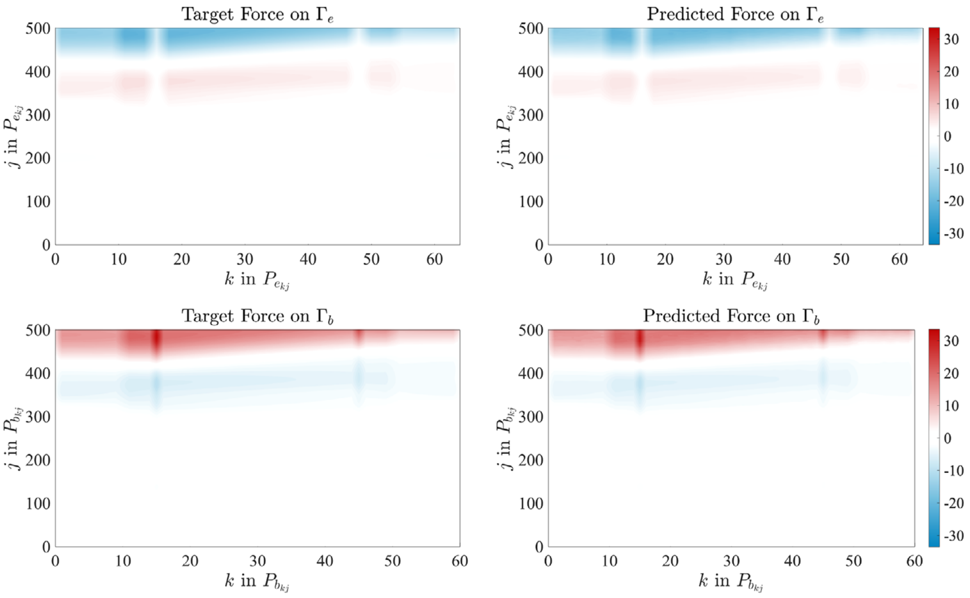

FIGURE 18 DRM force identification using our CNN in Example 2 (the best case of $\mathcal{E}$ of 0.22%).

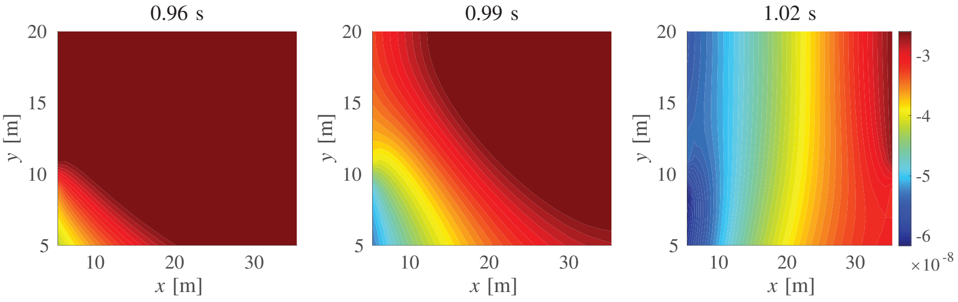

(A) Target Response

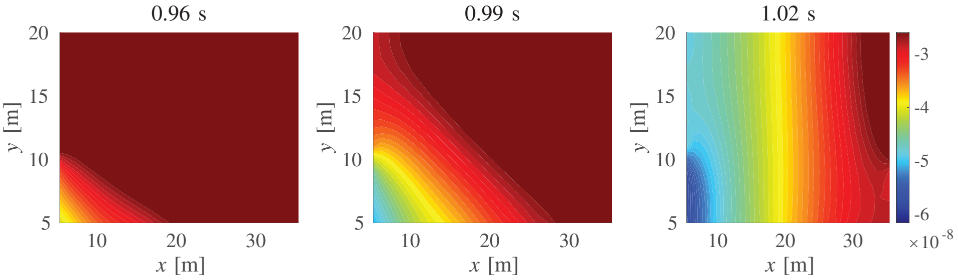

(B) Predicted Response

FIGURE 19 Wave response (u) reconstruction using the identified DRM force shown in Figure 18 in Example 2 shown at three distinct timesteps (the best case of $\mathcal{E}^u$ of 0.20%).

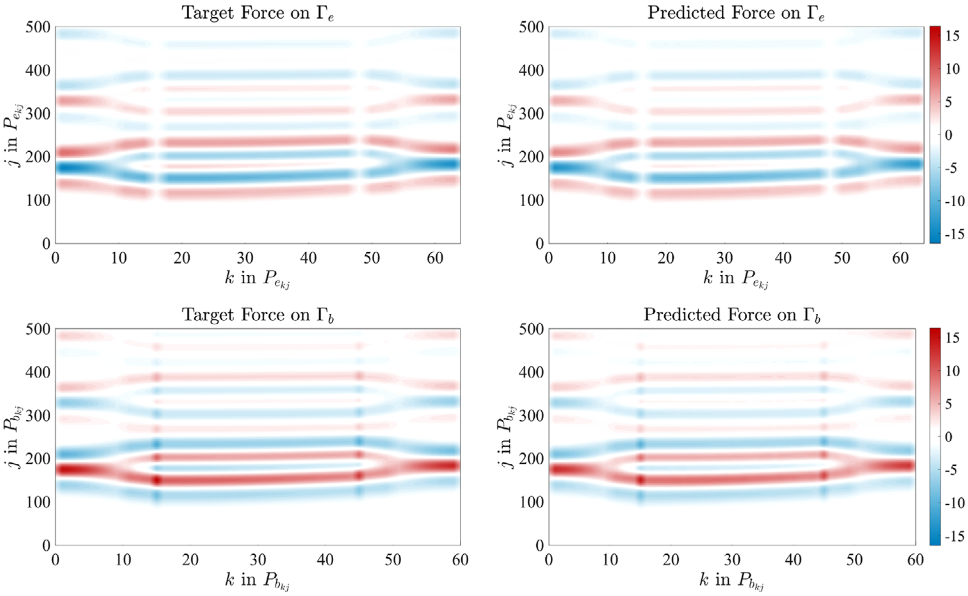

FIGURE 20 DRM force identification at the 50th percentile using our CNN in Example 2 ($\mathcal{E}$ of 1.12%).

lengths can appear unequal because they must terminate at observed data points, even though the 1.5 IQR distance is the same on both sides. Any data points beyond the boundaries of these whiskers are displayed as outliers. The use of 1.5 times the IQR is a common convention in box-and-whisker plots for identifying potential outliers. Any error that falls below the minimum whisker or above the maximum whisker is classified as an outlier and is marked with a red "+" symbol.

Herein, we evaluated different CNN models, each of which is adjusted for each number of sensors, for site profile 1. Among them, the CNN model using 31 sensors in the input layer demonstrated impressive performance. Specifically, when we tested it with 2000 test data points, it successfully identified targeted DRM forces for over 92% of the test data within the 5% $\mathcal{E}$ threshold. In contrast, the CNN models trained with only 5–15 sensors fell short of achieving the same

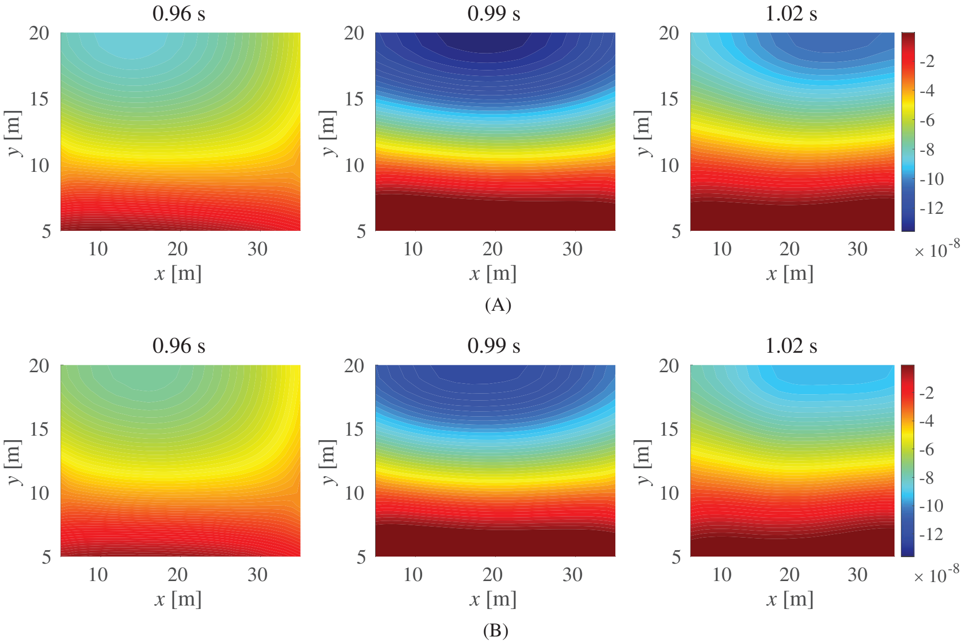

FIGURE 21 Wave response (u) reconstruction using the identified DRM force shown in Figure 20 (the 50th percentile) in Example 2 shown at three distinct timesteps ($\mathcal{E}^u$ of 0.82%). (A) Target response. (B) Predicted response.

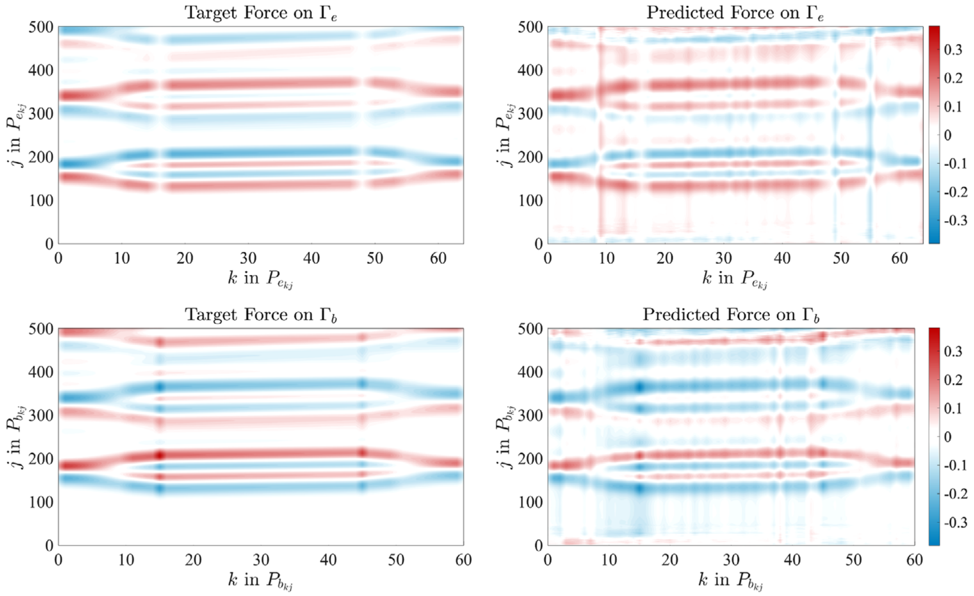

FIGURE 22 The poorest DRM force identification using our CNN in Example 2 ($\mathcal{E}$ of 24.52%).

level of accuracy, with less than 90% of the test data meeting the 5% $\mathcal{E}$ threshold. Additionally, when we conducted a similar numerical investigation for site profile 2, we noticed that the CNN model trained with 31 sensors excelled by successfully identifying targeted DRM forces for more than 95% of the test data within the 5% $\mathcal{E}$ threshold. In contrast, the other three models, achieved to identify targeted DRM forces for slightly under 92% of the test data set within the $\mathcal{E}$ threshold.

We also found that, when we used a model trained with data from 31 sensors, it outperformed the others in handling atypical cases, suggesting that the CNN trained with more sensor data was better equipped to deal with variations in the data distribution. Namely, using 31 sensors resulted in fewer outliers than the other cases in site profiles, as depicted in Table 3.

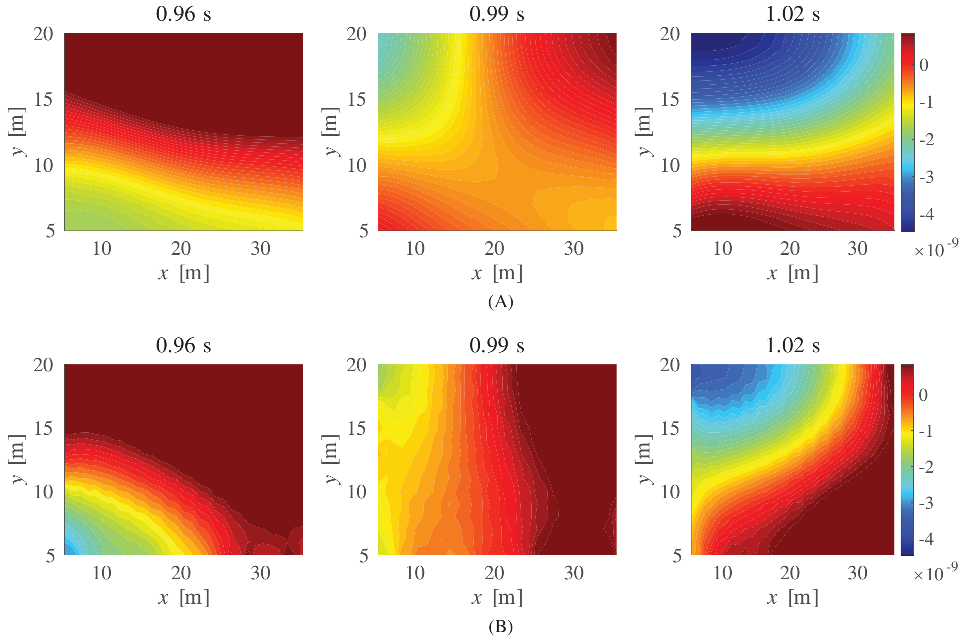

FIGURE 23 Wave response (u) reconstruction using the identified DRM force shown in Figure 22 (the highest error) in Example 2 shown at three distinct timesteps ($\mathcal{E}^u$ of 29.79%). (A) Target response. (B) Predicted response.

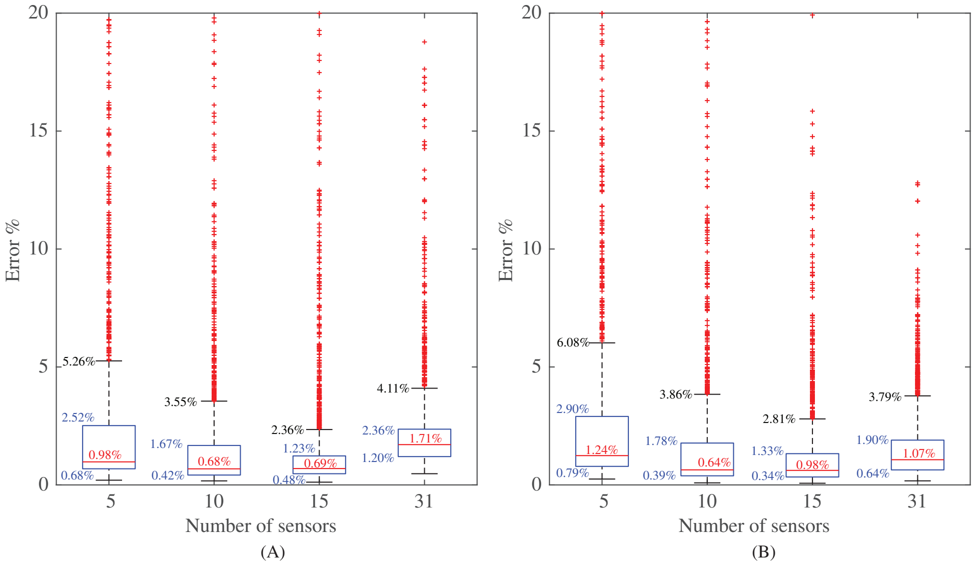

FIGURE 24 Reconstruction error ($\mathcal{E}$) distribution across the 2000 test data set using different number of sensors for homogeneous and heterogeneous domains, respectively. (A) Homogeneous domain (site profile 1). (B) Heterogeneous domain (site profile 2).

TABLE 3 Table listing the number of outliers in the force reconstruction error ($\mathcal{E}$) using a different number of sensors.

	Number of outlier $\mathcal{E}$ samples	
Sensors	**Site profile 1 (Figure 24A)**	**Site profile 2 (Figure 24B)**
5 sensors	311	255
10 sensors	251	224
15 sensors	292	221
31 sensors	186	185

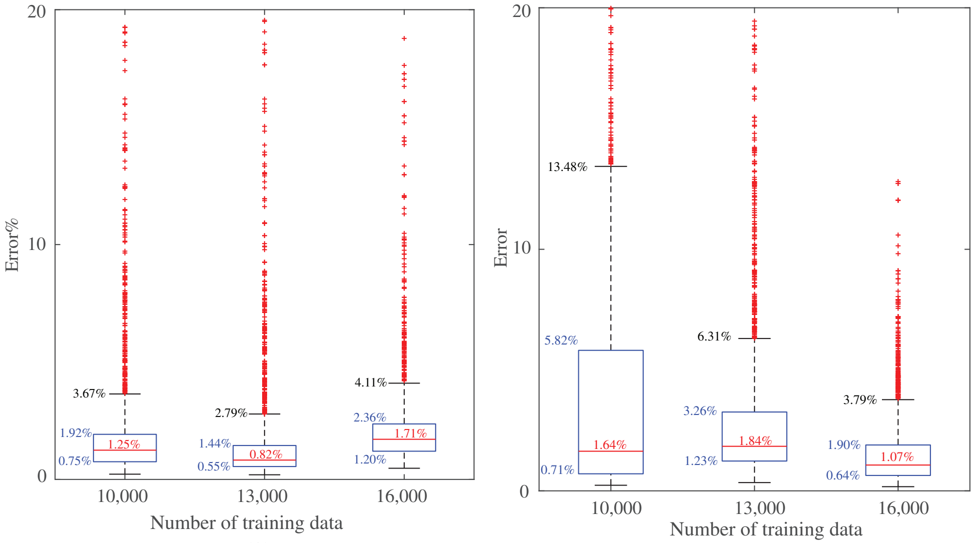

(A) (B)

FIGURE 25 Reconstruction error ($\mathcal{E}$) distribution across the 2000 test data set using different number of training data samples for homogeneous and heterogeneous domains, respectively. (A) Homogeneous domain (site profile 1). (B) Heterogeneous domain (site profile 2).

TABLE 4 Table listing the number of outliers in the force identification error ($\mathcal{E}$) using different number of training data.

	Number of outlier $\mathcal{E}$ samples	
Training data	**Site profile 1 (Figure 25A)**	**Site profile 2 (Figure 25A)**
10,000	253	221
13,000	287	230
16,000	186	185

5.3.2 | Performance of the CNN with respect to the number of training data samples

We also investigate how the amount of training data affects the performance of CNN models for both homogeneous and heterogeneous domains. It is a common expectation in machine learning that exposing the model to more training data should lead to improved performance on test data, and we examine whether a similar trend occurs in our experiments.

We demonstrate that the CNN model using a training data set of 16,000 samples produces better reconstruction results compared to the other CNN models trained with 10,000 and 13,000 samples. For the homogeneous domain, the model trained on 16,000 samples can identify targeted DRM forces for 92% of the 2000 test data points within a 5% $\mathcal{E}$ threshold. In contrast, the other two models, trained with fewer samples, can identify targeted DRM forces for only about 90% of the test data within the same $\mathcal{E}$ threshold.

For the heterogeneous domain, we find that the model trained on 16,000 samples excels, identifying targeted DRM forces for more than 95% of the 2000 test data points within a 5% $\mathcal{E}$ threshold. However, the models trained on 13,000 and 10,000 samples struggle in this scenario, managing to identify targeted DRM forces for only 85 and 72% of the test data within the 5% $\mathcal{E}$ threshold, respectively. We also found that the predictions made by the 16,000-sample model have fewer outliers than the other cases, as indicated in Table 4. This finding supports that using a larger training data set (16,000 samples) and a greater number of sensors (31 sensors) improves the model's ability to generalize and handle atypical test data better than models with fewer samples and sensors, leading to less outliers.

5.4 | Example 4: Blind test mimicking a case when our CNNs resort to realistic earthquakes

We test the performance of the CNNs, which were already trained and showed its performance in Examples 1 and 2, for a test, mimicking a realistic seismic-event scenario. For instance, the presented method copes with incident seismic waves

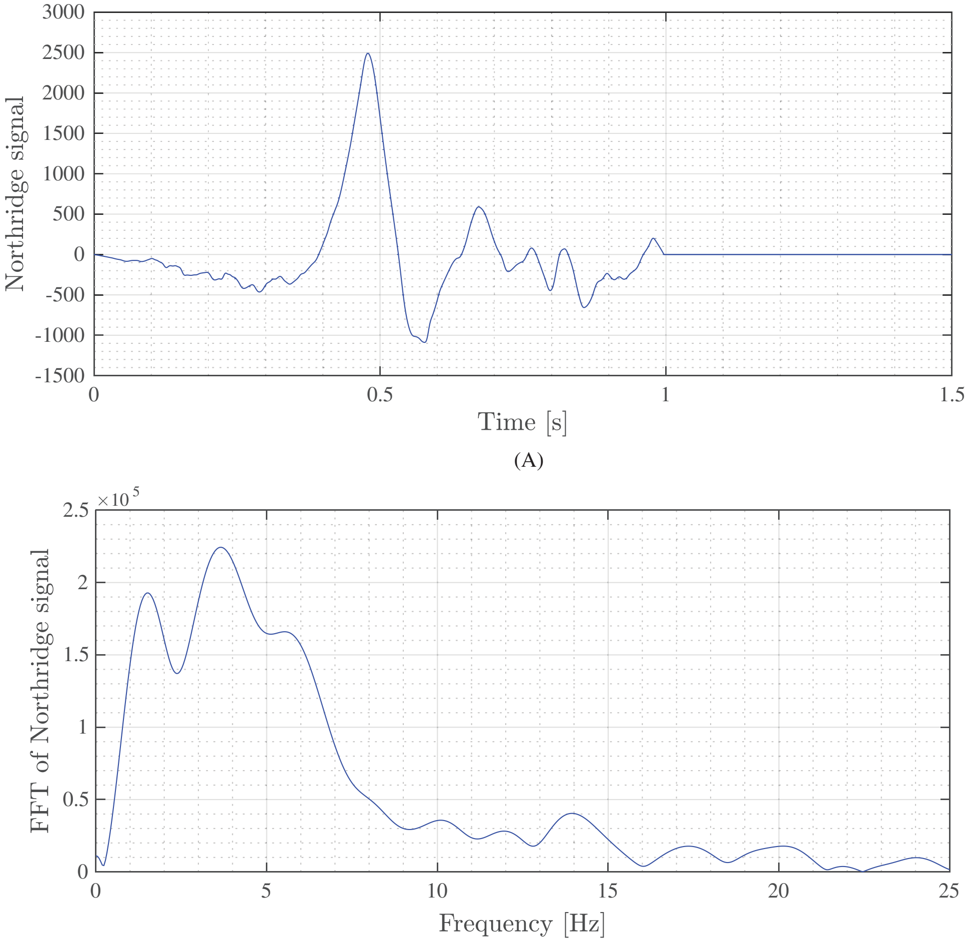

(A)

(B)

FIGURE 26 The source's excitation signal used in the enlarged-domain FE simulation in Example 4. (A) Time history of the Northridge signal used in Example 4. (B) Frequency content of the Northridge earthquake ground motion signal used in Example 4.

of unpredicted waveforms. Namely, the overall source profile in this new test has not been considered when we generated in the training data in Examples 1 and 2, and it is quite different from those for the training data. More specifically, in Example 4, we generate so-called "blind" test data that the training process has not experienced before in the following manner so that, via this new test, we avoid an "inverse crime."

- The hypocenter is in the furthest point away from the interior domain (i.e., even farther than the hypocenter used for the training data). To this end, we locate the point wave source location at $x^s = 20$ m and $y^s = 20$ m (i.e., the lower-left corner in the enlarged domain).
- The source's excitation signal is a part of a real earthquake ground-motion signal (the early-peak part of a ground motion signal measured during the 1994 Northridge earthquake), which is compressed into the simulation duration, as shown in Figure 26. We note that a realistic earthquake ground motion signal is utilized as the source signal to generate the wave motions in the enlarged domain so that the corresponding DRM forces may represent a more realistic and more complex incident waveform than those in the training data.
- We acknowledge that, in the real applications, the measurement sampling rate is inherently discrete and coarse while the real physics response is a continuous function over time. To mimic such a realistic setting in a computational study, this Example 4 uses the FE simulation with a much finer time step of 0.001 s than the sampling rate of 0.003 s. As a result, the predicted DRM force is produced at every 0.003 s while the targeted DRM force is defined at every 0.001 s.

Figure 27 presents the targeted wave responses at three distinct time steps in the enlarged domain in this blind test. Table 5 shows the values of $\mathcal{E}$ and $\mathcal{E}^u$ obtained by CNNs trained on homogeneous and heterogeneous truncated domains,

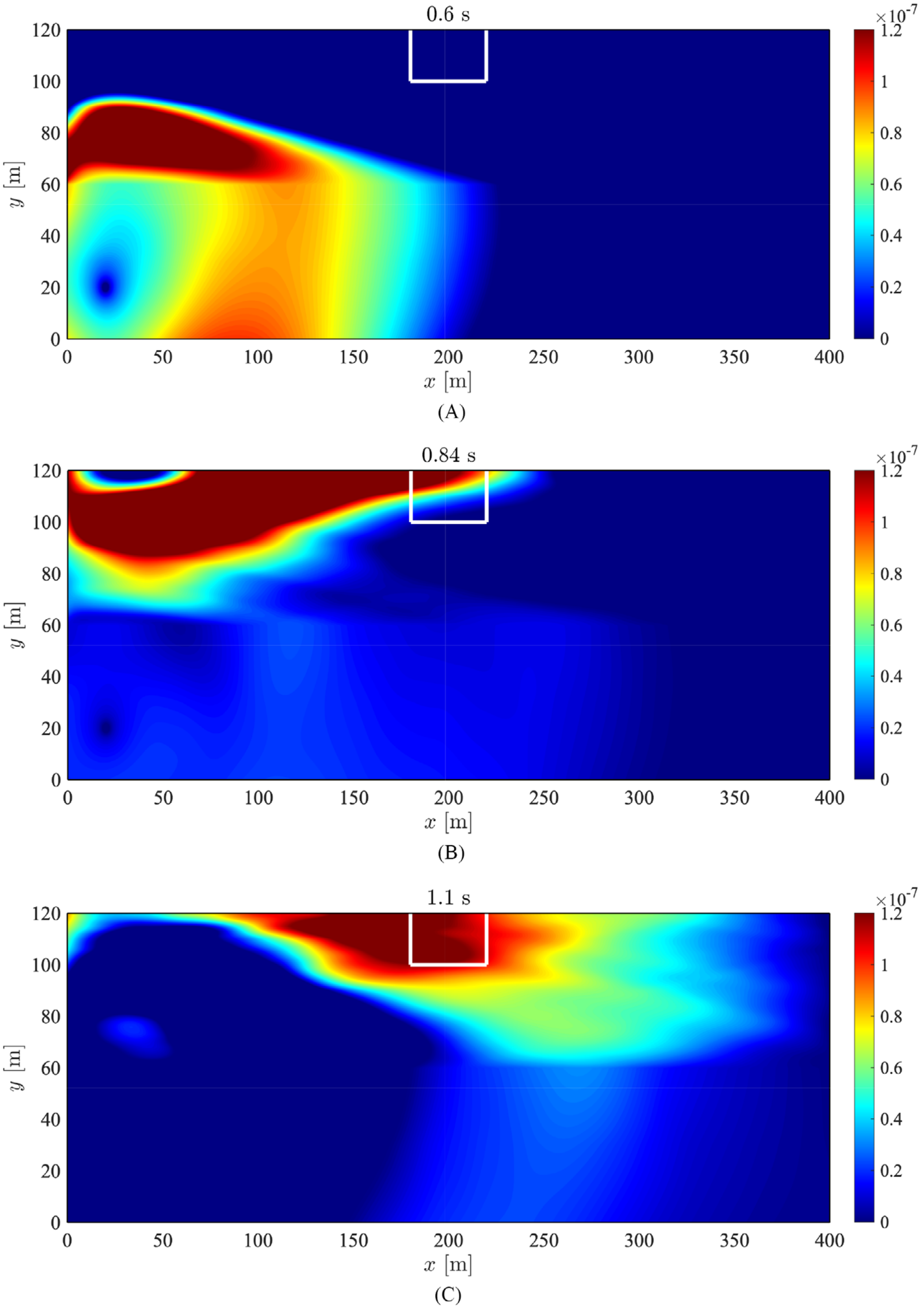

FIGURE 27 Target wave responses (u) in the enlarged domain at three distinct time steps in Example 4. The white solid lines in the middle of the top surface area delineate the reduced domain of interest. (A) Target response in the enlarged domain at 0.6 s. (B) Target response in the enlarged domain at 0.84 s. (C) Target response in the enlarged domain at 1.1 s.

TABLE 5 Table listing force and response reconstruction error ($\mathcal{E}$ and $\mathcal{E}^u$, respectively) in percentage in Example 4.

	$\mathcal{E}$	$\mathcal{E}^u$
Homogeneous soil (site profile 1)	1.31%	1.45%
Heterogeneous soil (site profile 2)	0.67%	0.68%

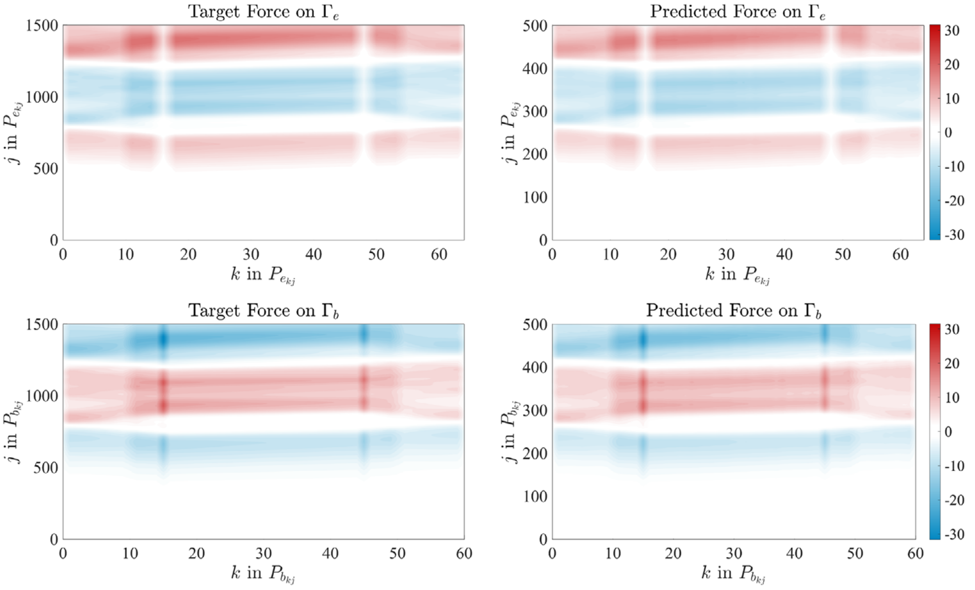

FIGURE 28 DRM force identification for the heterogeneous profile ($\mathcal{E}$ of 0.67%) in Example 4.

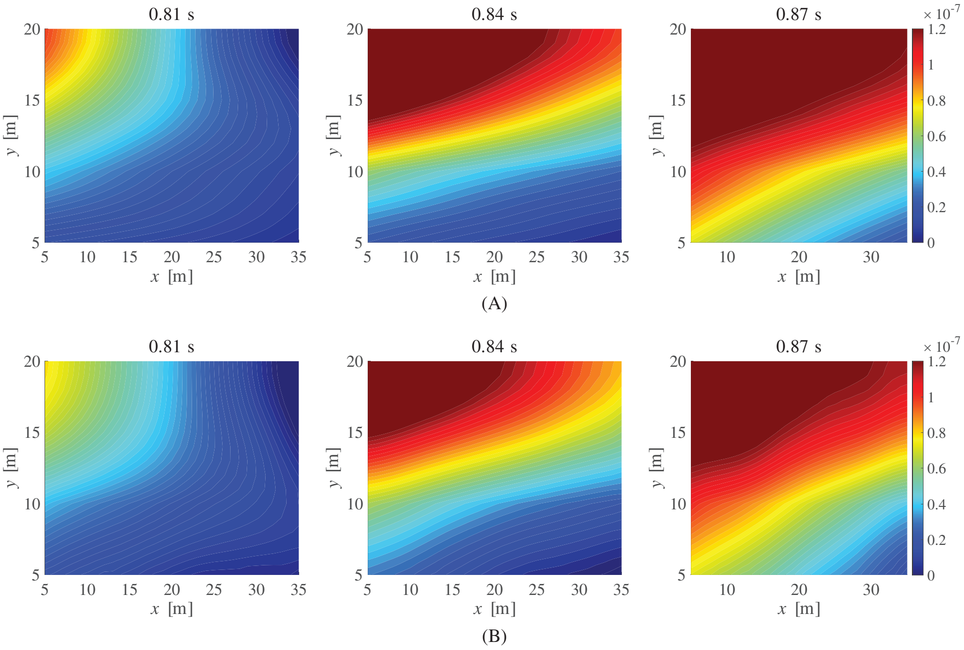

(A)

(B)

FIGURE 29 Wave response (u) reconstruction using the identified DRM force shown in Figure 28 at three distinct timesteps ($\mathcal{E}^u$ of 0.68%) in Example 4. (A) Target response. (B) Predicted response.

respectively. To compute $\mathcal{E}$ and $\mathcal{E}^u$ in the case when the sampling rate of the sensors (i.e., 0.003 s) differ from the time step (i.e., 0.001 s) of the enlarged-domain FE simulation of the blind test data, we conduct the following. First, we compare the CNN-identified DRM forces and their targets at every 0.003 s. Second, the wave responses are reconstructed by using the DRM wave solver with the time step of 0.003 s and the CNN-predicted DRM forces, and, in turn, they are compared at every 0.003 s with the targeted wave responses from the FE simulation with the time step of 0.001 s. For the homogeneous truncated domain, the error $\mathcal{E}$ for DRM force identification is 1.31%, and the error $\mathcal{E}^u$ for wave response reconstruction is 1.45%. On the other hand, for the heterogeneous case, the errors were $\mathcal{E} = 0.67\%$ (Figure 28) and $\mathcal{E}^u = 0.68\%$ (Figure 29), respectively. When comparing the results obtained in realistic earthquake scenarios with those obtained in Examples 1 and 2, it is noteworthy that the error values, $\mathcal{E}$ and $\mathcal{E}^u$, obtained in Example 4 are even smaller than the 25th percentile

TABLE 6 Error $\mathcal{E}$ in the inverted DRM forces and error $\mathcal{E}^u$ in the reconstructed wave responses obtained when using the presented CNN method versus the PDE-constrained optimization approach by Guidio et al.[22].

		$\mathcal{E}$		$\mathcal{E}^u$	
	CNN's performance in Examples 1 and 2	**CNN**	**PDE-opt.**	**CNN**	**PDE-opt.**
Example 1: Site profile 1	Best	0.73%	4.85%	0.69%	1.71%
	Median	2.01%	9.77%	1.58%	1.68%
Example 2: Site profile 2	Best	0.22%	0.67%	0.20%	0.20%
	Median	1.12%	7.36%	0.82%	0.35%

of their corresponding counterparts in Examples 1 and 2. It is remarkable that the errors in such an entirely blind test are very small. It suggests that the CNNs trained by the presented methodology can be effectively utilized for completely blind realistic tests in complex and realistic wave settings.

6 | DISCUSSION

6.1 | Comparison between the presented ML method and the PDE-constrained optimization

In this section, we compare the inversion performance of the presented data-informed CNN approach with that of the PDE-constrained optimization method shown by Guidio et al.[22] We use the test data that correspond to the best and the median performance obtained by the CNNs in Examples 1 and 2 to highlight the differences of the inversion performance between the presented CNN and the PDE-constrained optimization. For each case, we utilize the measured displacement fields of wave motions ($\mathbf{u}^{\mathrm{m}}$) as input data in the PDE-constrained optimization algorithm, which will identify the target DRM forces. Table 6 summarizes the values of $\mathcal{E}$ and $\mathcal{E}^u$ obtained through each approach.

As shown in Table 6, for the test data sets corresponding to the best and median performance of the CNNs in Examples 1 and 2, the error $\mathcal{E}$ obtained by the PDE-constrained optimization method is greater than the former, while $\mathcal{E}^u$ is comparable in both methods. For instance, Figure 30 shows the target DRM forces, as well as DRM forces identified by CNN and by the optimization algorithm for the case of median performance of the CNN in Example 1. For this case, the CNN can identify the DRM forces with an error $\mathcal{E}$ of 2.01%, while $\mathcal{E}$ of 9.77% is obtained from the PDE-constrained optimization algorithm. Overall, in most cases, the performance, in terms of $\mathcal{E}$, of the CNN is better than the PDE-constrained optimization method.

Additionally, the CNN offers a significant advantage over the PDE-constrained optimization method in terms of processing time. In the provided examples, the CNN takes 0.15 s for each single test data set, whereas the PDE-constrained optimization method takes about an hour for the same data set. Moreover, as we move to vector waves and a 3D setting, the processing time of the PDE-constrained optimization would become much longer, while the ML-based approach would still remain in the scale of a second.

6.2 | Is the presented ML method accurate for the energy assessment?

When using ML methods to simulate or predict physical systems, it is crucial to evaluate whether the ML-predicted wave responses in a system adhere to the principles of energy conservation. Failing to do so can lead to incorrect assessment of seismic behaviors of built environments. Therefore, in this particular example, we evaluate the ability of the proposed data-informed CNN approach to ensure the conservation of energy.

Figure 31 compares the total energy in the system over time generated by the CNN-predicted DRM force that correspond to the median performance in the test data in Examples 1 and 2 and their corresponding target counterparts. The CNN-identified forces for the median performance in Example 1 generate a slightly larger energy in the system over time than their targeted counterparts (as shown in Figure 31A), while those in Example 2 cause a slightly lower energy over time than targets (as indicated in Figure 31B). These discrepancies in total energy in the domain originate from marginal inaccuracies in the identified forces by the data-informed CNN model.

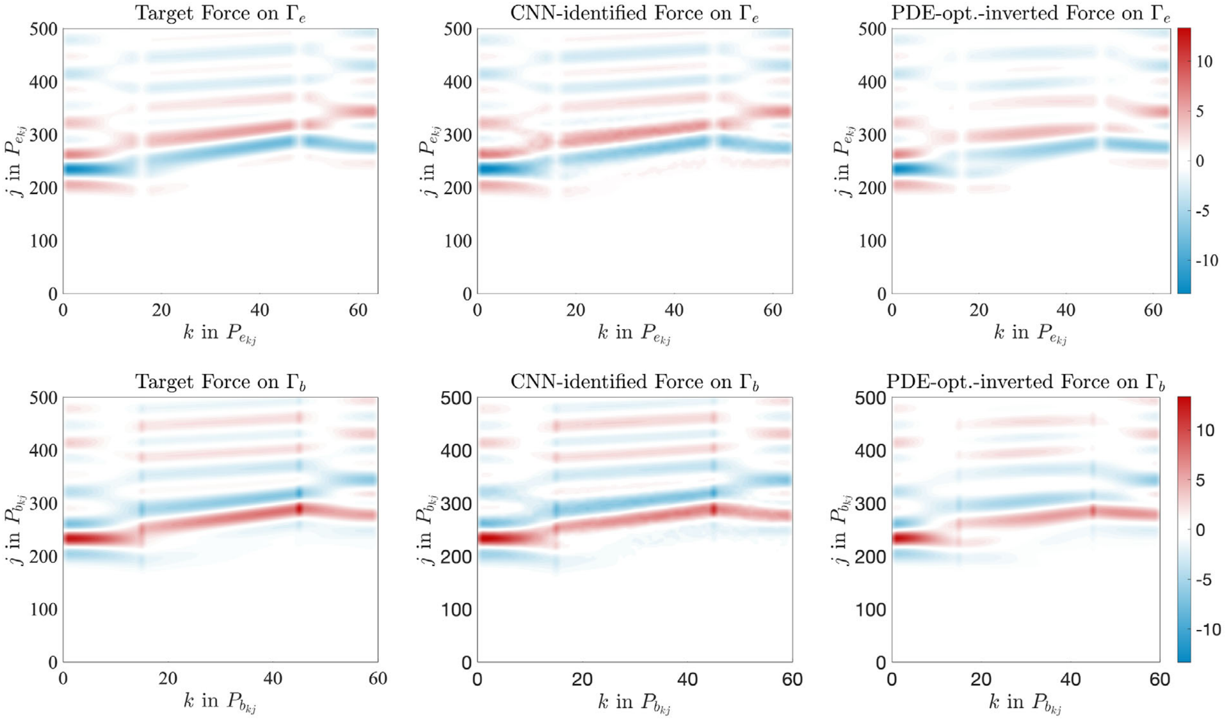

FIGURE 30 (Left) Target, (middle) CNN-identified, and (right) PDE-constrained optimization-inverted DRM forces for the case of median performance of the CNN in Example 1.

7 CONCLUSIONS

Our study demonstrates the effectiveness of using CNNs to accurately identify effective seismic forces at a DRM layer in a truncated domain for rapid reconstruction of SH ground motions by using sparsely made seismic measurement data. The overall architecture of our CNN model, along with the rationale behind the filter and layer specifications, contributes to the effective extraction and representation of the underlying features within the input-layer feature data, culminating in improved performance and capabilities for predicting the output-layer feature data. Our findings indicate the CNN's strong capability in accurately identifying DRM forces, offering great potential for reconstructing wave responses in a domain of interest. We also found that using a larger data set and a greater number of sensors improves the model's ability to generalize and handle atypical test data better than models with fewer samples and sensors. We also compared the performance of the presented CNN method to that of an existing contender that is based on the PDE-constrained optimization. Our analysis shows that the CNN takes a very short processing time while it outperforms the PDE-constrained optimization method in terms of the accuracy of the DRM-force identification in the presented examples under the SH wave setting. Specifically, the merits of the presented method are summarized as follows.

- High-efficiency inference: The scale of the ratio between the dimensions of the input layer data (seismic measurements) and the output layer data (DRM forces across all the nodes at the DRM layer) can be 10:126 (or around 1:12) when employing, for instance, 10 sensors, as demonstrated in our presented examples. Consequently, the ratio between the size of the measurement data and the reconstructed wave response data within the interior domain stands at 10:496 (about 1:49). Building upon this highly effective inference, we propose that the robustness of this method is attributed to its effective utilization of these sparsely distributed measurement data.
- Overcoming the 1D limit of deconvolution: The presented data-informed CNN method can infer DRM forces (or incident waves) on all the nodes at the DRM layer from the sparse measurement data in a multidimensional setting even in the presence of incoherent waves. Thus, or method is not limited to plane waves, unlike the conventional approaches, such as deconvolution, and it is applicable to azimuthally arbitrary incident waves.
- Faster processing speed than the PDE-constrained optimization: The CNN presented in this study boasts an exceptionally rapid processing time, typically taking less than a second. In comparison, the PDE-constrained optimization

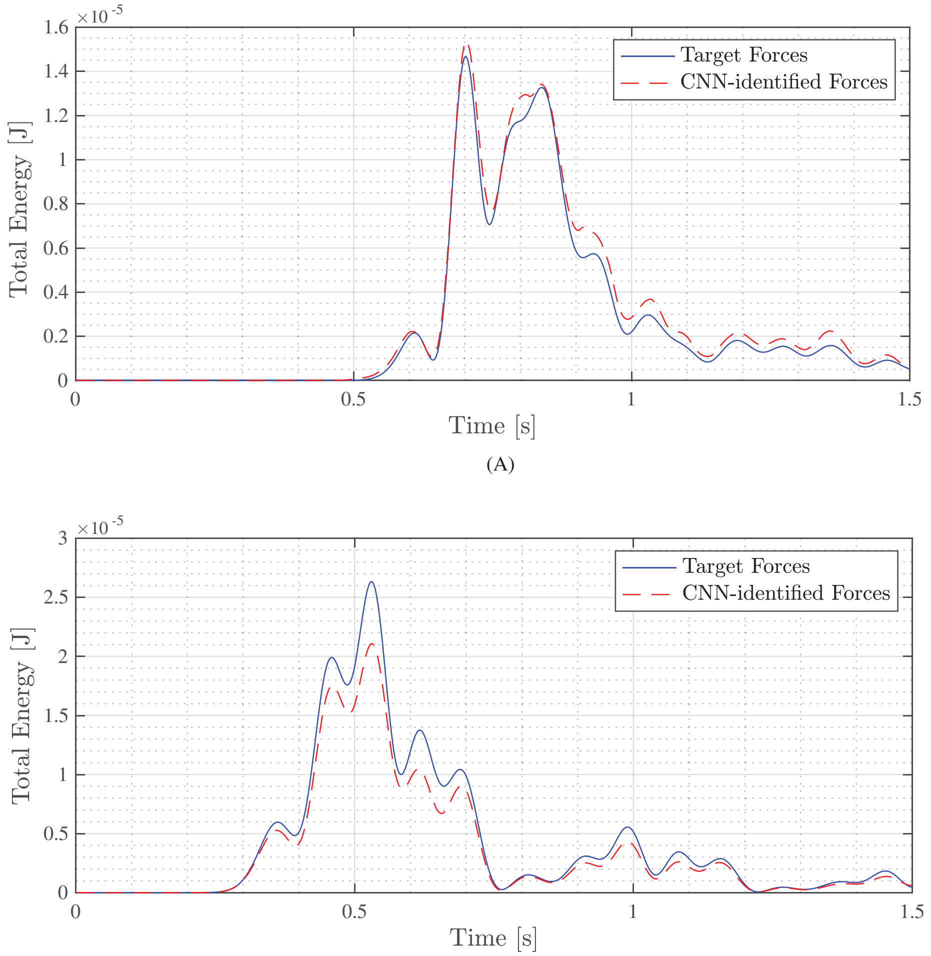

(A)

(B)

FIGURE 31 Comparison of total energy generated by target and CNN-identified forces that correspond to the median performance of the CNN in Examples 1 and 2. (A) Time history of the total energy for the case of median performance of the CNN in Example 1. (B) Time history of the total energy for the case of median performance of the CNN in Example 2.

approach, which is reported to identify DRM forces in the same 2D problem, often requires hours to yield results. This remarkable gain of the processing speed of the CNN is particularly noteworthy when considering the substantial size of the input and output layer feature data, with examples showcasing a sample size as large as 501 time steps × 126 DRM nodes, totaling 63,126 discrete output data points. Furthermore, as we contemplate extending this methodology to accommodate vector waves within a 3D setting, the processing time of the PDE-constrained optimization approach is anticipated to grow substantially. Conversely, the ML-based approach will remain remarkably quick, still completing its tasks in just seconds. Consequently, this work underscores the potential of ANNs as effective and efficient tools, even for more complex and larger-scale problems in 3D elastic wave settings.

Further research may explore this ML-based DRM force inversion approach for vector waves in 2D and 3D settings. Expanding the proposed approach to 3D settings allows earthquake engineers to simulate the impact of earthquakes on built environments, including subsurface systems such as foundations and underground structures, and surrounding soils. For instance, a DRM-powered 3D wave solver that can incorporate various topography settings and realistic buildings would take advantage of extensive seismic measurement data from built environments equipped with modern sensors (e.g., distributed acoustic sensors (DAS),[44] or vision-based motion sensors[45]). The presented method could also be extended to consider the nonlinearity of soils, given that near-surface soils can exhibit nonlinear response behavior during moderate and strong earthquakes. Accordingly, the data-informed CNN method would consider the soil's nonlinear behavior during data generation for training as the DRM is capable of modeling nonlinearities.[46] This method can aid decision-makers in quickly assessing the structural integrity of infrastructure after an earthquake.

ACKNOWLEDGMENTS

This material is based upon work supported by the National Science Foundation, under Award CMMI-2053694. Any opinions, findings, and conclusions or recommendations expressed in this material are those of the authors and do not necessarily reflect the views of the National Science Foundation. The authors are also grateful for the support by the Faculty Research and Creative Endeavors (FRCE) Research Grant-48058 at Central Michigan University. The authors express their gratitude to the PSC-Bridges supercomputer resource for enabling the accomplishment of this research. Additionally, this study made use of the Extreme Science and Engineering Discovery Environment (XSEDE), which is made possible through the support of National Science Foundation Grant Number ACI-1548562. Specifically, the Bridges-2 system, supported by NSF award number ACI-1928147 at the Pittsburgh Supercomputing Center (PSC), played a crucial role in the execution of this work.

CONFLICT OF INTEREST STATEMENT

The authors declare no conflicts of interest.

DATA AVAILABILITY STATEMENT

The data that support the findings of this study are available from the corresponding author upon reasonable request.

ORCID

Bruno Guidio https://orcid.org/0000-0003-1943-8806
Chanseok Jeong https://orcid.org/0000-0002-0488-8559

REFERENCES

1. Ju SH. A Deconvolution scheme for determination of seismic loads in finite element analyses. *Bull Seismol Soc Am*. 2013;103(1):258-267. doi: 10.1785/0120120034
2. Poul MK, Zerva A. Efficient time-domain deconvolution of seismic ground motions using the equivalent-linear method for soil-structure interaction analyses. *Soil Dyn Earthq Eng*. 2018;112:138-151.
3. Poul MK, Zerva A. Nonlinear dynamic response of concrete gravity dams considering the deconvolution process. *Soil Dyn Earthq Eng*. 2018;109:324-338. doi: 10.1016/j.soildyn.2018.03.025
4. Mánica MA, Pinzón LA, Pujades LG, Hidalgo-Leiva DA, Ordaz MG. Time domain deconvolution in nonlinear elastoplastic soil deposits. *Soil Dyn Earthq Eng*. 2023;172:107993.
5. Akcelik V, Biros G, Ghattas O. Parallel multiscale Gauss-Newton-Krylov methods for inverse wave propagation. In: IEEE; 2002:41.
6. Akcelik V, Bielak J, Biros G, et al. High resolution forward and inverse earthquake modeling on terascale computers. In: IEEE; 2003:52.
7. Ghahari S, Abazarsa F, Taciroglu E. Probabilistic blind identification of site effects from ground surface signals. *Bull Earthq Eng*. 2018;16:1079-1104.
8. Ghahari S, Abazarsa F, Jeong C, Kurtulus A, Taciroglu E. Blind identification of site effects and bedrock motion from surface response signals. *Soil Dyn Earthq Eng*. 2018;107:322-331. doi: 10.1016/j.soildyn.2018.01.045
9. Ghahari F, Abazarsa F, Ebrahimian H, Zhang W, Arduino P, Taciroglu E. Identification of nonlinear soil properties from downhole array data using a Bayesian model updating approach. *Sensors*. 2022;22(24):9848. doi: 10.3390/s22249848
10. Ebrahimian H, Taha A, Ghahari F, Asimaki D, Taciroglu E. Estimation of soil–structure model parameters for the Millikan library building using a sequential Bayesian finite element model updating technique. *Buildings*. 2022;13(1):28. doi: 10.3390/buildings13010028
11. Li G, Xue Y, Wang R, Zhang H, Dong Z, Yu D. Multiphase wavefield inversion methodology for seismic analysis of soil-structure interaction systems. *Soil Dyn Earthq Eng*. 2023;173:108081. doi: 10.1016/j.soildyn.2023.108081
12. Guidio B, Jeremić B, Guidio L, Jeong C. Passive seismic inversion of SH wave input motions in a truncated domain. *Soil Dyn Earthq Eng*. 2022;158:107263. doi: 10.1016/j.soildyn.2022.107263
13. Roësset JM, Chang DW, Stokoe KH, Aouad M. Modulus and thickness of the pavement surface layer from SASW tests. *Transp Res Rec*. 1990;1260:53-63.
14. Luke BA, Stokoe KH. Application of SASW method underwater. *J Geotech Geoenviron Eng*. 1998;124(6):523-531. doi: http://doi.org/10.1061/(ASCE)1090-0241(1998)124:6(523)
15. Brown LT, Boore DM, Stokoe KH. Comparison of shear-wave slowness profiles at 10 strong-motion sites from noninvasive SASW measurements and measurements made in boreholes. *Bull Seismol Soc Am*. 2002;92(8):3116-3133.
16. Cox BR, Teague DP. Layering ratios: a systematic approach to the inversion of surface wave data in the absence of a priori information. *Geophys J Int*. 2016;207(1):422-438.
17. Teague DP, Cox BR, Rathje EM. Measured vs. predicted site response at the Garner Valley Downhole Array considering shear wave velocity uncertainty from borehole and surface wave methods. *Soil Dyn Earthq Eng*. 2018;113:339-355.
18. Park CB, Miller RD, Xia J. Multichannel analysis of surface waves. *Geophysics*. 1999;64(3):800-808.
19. Rahimi S, Wood CM, Himel AK. Application of microtremor horizontal to vertical spectra ratio (MHVSR) and multichannel analysis of surface wave (MASW) for shallow bedrock mapping for transportation projects. In: *Geo-Congress 2020*. American Society of Civil Engineers; Reston, VA; 2020:622-632.

20. Fathi A, Kallivokas LF, Poursartip B. Full-waveform inversion in three-dimensional PML-truncated elastic media. *Comput Methods Appl Mech Eng*. 2015;296:39-72.
21. Fathi A, Poursartip B, Stokoe KH, Kallivokas LF. Three-dimensional P-and S-wave velocity profiling of geotechnical sites using full-waveform inversion driven by field data. *Soil Dyn Earthq Eng*. 2016;87:63-81.
22. Guidio B, Goh H, Jeong C. Effective seismic force retrieval from surface measurement for SH-wave reconstruction. *Soil Dyn Earthq Eng*. 2023;165:107682. doi: http://doi.org/10.1016/j.soildyn.2022.107682
23. Bielak J, Loukakis K, Hisada Y, Yoshimura C. Domain reduction method for three-dimensional earthquake modeling in localized regions, Part I: Theory. *Bull Seismol Soc Am*. 2003;93(2):817-824.
24. Yoshimura C, Bielak J, Hisada Y, Fernández A. Domain reduction method for three-dimensional earthquake modeling in localized regions, part II: verification and applications. *Bull Seismol Soc Am*. 2003;93(2):825-841.
25. Jeremić B, Jie G, Preisig M, Tafazzoli N. Time domain simulation of soil–foundation–structure interaction in non-uniform soils. *Earthq Eng Struct Dyn*. 2009;38(5):699-718.
26. Jeremić B, Tafazzoli N, Ancheta T, Orbović N, Blahoianu A. Seismic behavior of NPP structures subjected to realistic 3D, inclined seismic motions, in variable layered soil/rock, on surface or embedded foundations. *Nucl Eng Des*. 2013;265:85-94.
27. Poursartip B, Fathi A, Kallivokas LF. Seismic wave amplification by topographic features: a parametric study. *Soil Dyn Earthq Eng*. 2017;92:503-527. doi: http://doi.org/10.1016/j.soildyn.2016.10.031
28. Abell JA, Orbović N, McCallen DB, Jeremic B. Earthquake soil-structure interaction of nuclear power plants, differences in response to 3-D, 3× 1-D, and 1-D excitations. *Earthq Eng Struct Dyn*. 2018;47(6):1478-1495.
29. Poursartip B, Kallivokas LF. Model dimensionality effects on the amplification of seismic waves. *Soil Dyn Earthq Eng*. 2018;113:572-592. doi: http://doi.org/10.1016/j.soildyn.2018.06.012
30. Zhang L, Wang JT, Xu YJ, He CH, Zhang CH. A procedure for 3D seismic simulation from rupture to structures by coupling SEM and FEM. *Bull Seismol Soc Am*. 2020;110(3):1134-1148.
31. Sica S, Russo AD. Seismic response of large earth dams in near-source areas. *Comput Geotech*. 2021;132:103807.
32. Wang H, Yang H, Feng Y, Jeremić B. Modeling and simulation of earthquake soil structure interaction excited by inclined seismic waves. *Soil Dyn Earthq Eng*. 2021;146:106720.
33. Zhang W, Taciroglu E. 3D time-domain nonlinear analysis of soil-structure systems subjected to obliquely incident SV waves in layered soil media. *Earthq Eng Struct Dyn*. 2021;50(8):2156-2173.
34. Guidio B, Goh H, Kallivokas LF, Jeong C. On the reconstruction of the near-surface seismic motion. Submitted; 2023.
35. Nguyen KT, Kusanovic DS, Asimaki D. Three-dimensional nonlinear soil–structure interaction for Rayleigh wave incidence in layered soils. *Earthq Eng Struct Dyn*. 2022;51(11):2752-2770.
36. Rathod Y, Isbiliroglu Y, Nusbaumer O, et al. Development of the coupled soil-structure interaction (SSI) analysis model of a reactor building using domain reduction method (DRM). In: 26th International Conference on Structural Mechanics in Reactor Technology, 2022.
37. Gokhale NH. Solving an elastic inverse problem using Convolutional Neural Networks. *arXiv preprint arXiv:2109.07859*; 2021.
38. Vantassel JP, Kumar K, Cox BR. Using convolutional neural networks to develop starting models for near-surface 2-D full waveform inversion. *Geophys J Int*. 2022;231(1):72-90. doi: http://doi.org/10.1093/gji/ggac179
39. Stankevich A, Nechepurenko I, Shevchenko A, Gremyachikh L, Ustyuzhanin A, Vasyukov A. Learning velocity model for complex media with deep convolutional neural networks. *arXiv preprint arXiv:2110.08626*; 2021.
40. Wu Y, Lin Y, Zhou Z. InversionNet: accurate and efficient seismic waveform inversion with convolutional neural networks. In: SEG; 2018.
41. Maharjan S, Guidio B, Fathi A, Jeong C. Deep and convolutional neural networks for identifying vertically-propagating incoming seismic wave motion into a heterogeneous, damped soil column. *Soil Dyn Earthq Eng*. 2022;162:107510. doi: http://doi.org/10.1016/j.soildyn.2022.107510
42. Lysmer J, Kuhlemeyer RL. Finite dynamic model for infinite media. *J Eng Mech Div. ASCE*. 1969;95(EM4):859-877.
43. Pranto FM, Maharjan S, Jeong C. Level-Set and learn: convolutional neural network for classification of elements to identify an arbitrary number of voids in a 2D solid using elastic waves. *J Eng Mech*. 2023;149(6):04023035.
44. Daley TM, Freifeld BM, Ajo-Franklin J, et al. Field testing of fiber-optic distributed acoustic sensing (DAS) for subsurface seismic monitoring. *The Leading Edge*. 2013;32(6):699-706.
45. Ngeljaratan L, Moustafa MA. Structural health monitoring and seismic response assessment of bridge structures using target-tracking digital image correlation. *Eng Struct*. 2020;213:110551.
46. Kanellopoulos C, Psycharis N, Yang H, Jeremić B, Anastasopoulos I, Stojadinović B. Seismic resonant metamaterials for the protection of an elastic-plastic SDOF system against vertically propagating seismic shear waves (SH) in nonlinear soil. *Soil Dyn Earthq Eng*. 2022;162:107366.

How to cite this article: Maharjan S, Guidio B, Jeong C. Convolutional neural network for identifying effective seismic force at a DRM layer for rapid reconstruction of SH ground motions. *Earthquake Engng Struct Dyn*. 2024;53:894–923. https://doi.org/10.1002/eqe.4049